

1 **Revision 1**

2

Word Count: 6923

3 **In situ Raman vibrational spectra of siderite (FeCO₃) and rhodochrosite (MnCO₃)**

4

up to 47 GPa and 1100 K

5

6 *Chao Wang^{1,2}, Lu'an Ren^{2, 3}, Jesse B. Walters⁴, Lifei Zhang¹, Renbiao Tao², **

7

8 *¹School of Earth and Space Sciences, Peking University, Beijing 100871, China*

9

²Center for High Pressure Science and Technology Advanced Research (HPSTAR),

10

Beijing 100094, China

11

³School of Earth Science and Resources, China University of Geosciences (Beijing),

12

Beijing 100083, China

13

⁴Institut für Geowissenschaften, Goethe Universität, Frankfurt am Main 60438, Germany

14

* Corresponding author: renbiao.tao@hpstar.ac.cn

15

16

17

18

19

20

ABSTRACT

21 Siderite (FeCO_3) and rhodochrosite (MnCO_3) are two interesting carbonate minerals,
22 which normally occur in hydrothermal deposits on deep-sea altered oceanic crust. Despite
23 the ubiquity of carbonates in the slab, little is known of the physicochemical behavior of
24 siderite and rhodochrosite at high-pressure (P) and high-temperature (T) conditions
25 during slab subduction. In this study, we characterized the Raman vibrational spectra of
26 natural siderite and rhodochrosite up to 47 GPa and 1100 K in an externally-heated
27 diamond-anvil cell (DAC). Experimental results show that the Raman frequency shifts (ν_i)
28 for siderite and rhodochrosite are a function of both P and T , and the effect of the P - T
29 cross derivative term cannot be neglected, especially at high- P and high- T conditions.
30 Based on the functional relationship of ν_i - P - T , the P - T calibrants of siderite and
31 rhodochrosite are developed, respectively. This is significant for studying the
32 water-carbonate interaction at high P - T conditions in a DAC because the undesired
33 change of the experimental system from traditional pressure sensors (e.g., ruby, quartz) in
34 a reaction chamber can be avoided. Like previous studies, we observed a sharp spin
35 transition at ~ 45 GPa in siderite and a phase transition from MnCO_3 -I to MnCO_3 -II at \sim
36 46 GPa for rhodochrosite at room temperature. Furthermore, we determined the isobaric
37 and isothermal equivalents of the mode Grüneisen parameter (γ_{iT} , γ_{iP}) and the anharmonic
38 parameter (a_i) for each Raman mode of siderite and rhodochrosite. The $\delta\nu_i/\delta P$, $\delta\nu_i/\delta T$, γ_{iT} ,

39 γ_{iP} and a_i span a much larger value range for the external lattice modes (T, L) than internal
40 modes (ν_4, ν_1) in both siderite and rhodochrosite. Combining Raman frequency shifts and
41 the first-order Murnaghan equation of state, we also developed a method to calculate the
42 temperature dependence of the bulk modulus (K_T) for siderite and rhodochrosite,
43 respectively.

44

45 **Keywords:** Siderite, rhodochrosite, Raman spectroscopy, high- P and high- T , P - T sensor,
46 thermodynamical parameters.

47

48

49

1. INTRODUCTION

50 Carbonates are the major carbon reservoir on the Earth's surface. Previous studies
51 estimate that more than 6.5×10^8 Gt carbon have been stored in carbonate sediments and
52 carbonated oceanic/continental crusts (DePaolo 2015). These carbonates can be
53 transported into deep mantle through the subduction of oceanic/continental slabs (Javoy
54 1997; Dasgupta and Hirschmann 2006; Seto et al. 2008). With increasing depth in the
55 Earth's interior, some carbon may return to Earth's surface by all kinds of decarbonation
56 processes from subducted slabs through the magmas process (Stewart et al. 2019). The
57 stability of carbonates at high- P and high- T conditions controls the extent and rate of

58 carbon recycling to the Earth's surface. Therefore, knowing the physiochemical (e.g.,
59 thermodynamic) properties of carbonates at high P - T conditions relevant to subduction
60 zones is particularly important for understanding the deep carbon cycle process
61 (Dasgupta and Hirschmann 2010; Tao et al. 2013; Plank and Manning 2019; Farsang et al.
62 2020).

63 Siderite (FeCO_3) and rhodochrosite (MnCO_3) occur as common carbonate minerals
64 in many hydrothermal deposits on the altered oceanic crust (Robie et al. 1984).
65 Subduction of siderite and rhodochrosite may therefore play an important role in the
66 geochemical cycles of key elements (e.g. Fe, Mn, and C) between Earth's surface and
67 deep interior (Sherman 2009). On the other hand, previous studies have suggested
68 magnesite (MgCO_3) is the most important carbonate mineral in the deep Earth mantle,
69 which could be stable up to the P - T conditions of core-mantle boundary (Fiquet et al.
70 2002; Isshiki et al. 2004; Dasgupta and Hirschmann 2010). Considering the average
71 Fe/Mg molar ratio of ~ 0.12 in the bulk composition of Earth's mantle (McDonough and
72 Sun 1995), and the commonly occurring Fe-Mg exchange between carbonates and
73 Fe-bearing silicates at high- P and high- T conditions (Boulard et al. 2015), it is believed
74 that siderite (FeCO_3) should be a significant component in solid solution with magnesite
75 in the subducted slab and deep mantle (Anovitz and Essene 1987; Wood et al. 1996; Lin
76 et al. 2012; Tao et al. 2013; Kang et al. 2015). Similarly, divalent Mn has a cation size

77 between that of Mg^{2+} and Ca^{2+} , which could make rhodochrosite (MnCO_3) a non-trivial
78 endmember component in aragonite (CaCO_3) or dolomite [$\text{CaMg}(\text{CO}_3)_2$] at high P - T .
79 However, less attention has been paid to the physiochemical behavior of siderite and
80 rhodochrosite in comparison with calcite, dolomite, and magnesite, especially at high- P
81 and high- T conditions relevant to subduction zones and deep mantle environment.

82 More interestingly, Fe and Mn are 3d transition metals, which make siderite and
83 rhodochrosite have more complicated phase transitions and special spin states than other
84 carbonates at different chemical and P - T environments (Farfan et al. 2013; Litasov et al.
85 2020). For example, the stability of siderite and rhodochrosite have been determined as a
86 function of pressure, temperature, and oxygen fugacity by previous studies (Robie et al.
87 1984; Santillán and Williams, 2004; Tao et al. 2013; Kang et al. 2015; Litasov et al.
88 2020). In addition, the spin transition of siderite at room temperature was observed at 43
89 to 50 GPa, which results in a sharp isostructural volume collapse ranging from 6.5 % to
90 10 % (Nagai et al. 2010; Lin et al. 2012; Farfan et al. 2012; Müller et al. 2016).
91 Theoretically, if all thermodynamical data for different FeCO_3 and MnCO_3 phases at
92 high- P and high- T conditions are derived, the complete phase diagram for FeCO_3 and
93 MnCO_3 systems can be constructed. However, few experimental data are available at
94 simultaneous high P - T conditions (> 700 K) (e.g., Farsang et al. 2018, 2020). As a result,
95 the accurate thermodynamic properties of siderite and rhodochrosite are not well

96 contained at high P - T . For example, the bulk modulus parameter (K_T) of rhodochrosite at
97 high- T is not available, and the anharmonicity and anharmonic corrections have yet to be
98 quantified as well.

99 In this study, we studied the P - and T -induced frequency shifts of the Raman-active
100 vibrational modes of natural siderite ($\text{Fe}_{0.95}\text{Mn}_{0.046}\text{Mg}_{0.004}\text{CO}_3$) and rhodochrosite
101 ($\text{Mn}_{0.936}\text{Fe}_{0.059}\text{Mg}_{0.005}\text{CO}_3$) in a diamond-anvil cell (DAC) at pressures up to 47 GPa and
102 temperatures from 300 to 1100 K. To the best of our knowledge, this is the first
103 systematic report of simultaneous in situ high P - T Raman data for siderite and
104 rhodochrosite. Our results show that the frequency shifts of both siderite and
105 rhodochrosite are coupled functions of P and T . Based on in situ measurements, we
106 calculated the isobaric and isothermal equivalent of the Grüneisen parameter and the
107 anharmonic parameter and temperature-dependent bulk modulus for each vibrational
108 mode. Furthermore, we established P - T sensors according to their Raman-active modes,
109 which can be used to accurately determine the P in DAC at high- T and high- P conditions
110 (e.g., up to 15 GPa and 1100 K for siderite; up to 13 GPa and 900 K for rhodochrosite).
111 This is very useful for DAC experiments to study water-carbonate interaction (e.g.,
112 carbonate solubility in water) at the high P - T conditions relevant to subduction zones
113 while avoiding contamination by traditional pressure calibrants (e.g., ruby, SrB_4O_7 :
114 Sm^{2+}).

115

116

2. EXPERIMENTAL METHODS

117 The starting materials for the experiments are natural siderite (Ivigtut, Greenland)
118 and rhodochrosite (Wuzhou, China). They were characterized by electron microprobe and
119 Raman spectroscopy at the School of Earth and Space Sciences, Peking University. The
120 measurements yielded the molecular formula $(\text{Fe}_{0.95}\text{Mn}_{0.046}\text{Mg}_{0.004})\text{CO}_3$ and
121 $(\text{Mn}_{0.936}\text{Fe}_{0.059}\text{Mg}_{0.005})\text{CO}_3$ for siderite and rhodochrosite, respectively, indicating that the
122 starting siderite and rhodochrosite are close to the FeCO_3 and MnCO_3 end-members. For
123 simplification, we will refer to them as FeCO_3 and MnCO_3 in the rest of the text. Three
124 kinds of experiments (Atmospheric-*P* high-*T* experiments; Room-*T* and high-*P*
125 experiment; and High-*T* and high-*P* experiment) were conducted in this study.

126 The atmospheric-*P* (1 bar) high-*T* experiments were conducted up to 500 °C using
127 an HRTS1000 heating stage (Shanghai Photographic Instrument Co., Ltd) with the
128 sample held within the center of a heater coil on a sapphire pan. Before the
129 atmospheric-*P* high-*T* experiments, a series of calibration work was carried out to check
130 the temperature distribution in the center of the heater coil. Pure foils (0.5-1 mm in
131 diameter) of 63A solder, tin, zinc, and silver with known melting points of 183 °C,
132 232 °C, 420 °C and 961 °C, respectively, were heated in the sapphire pan. The
133 temperature of the sample position in the heater coil was determined by the instantaneous

134 shrinkage of the loaded metal foils at their melting point under a microscope (the
135 shrinkage duration was within 2s and the temperature interval was less than 0.1 °C). The
136 calibration was calculated using a linear fit of the four melting points of each foil
137 between 0 and 1000 °C. Repetition of the calibration procedure shows that the
138 temperatures are reproducible to less than $\pm 1^\circ\text{C}$. Following calibration, the formal
139 atmospheric-*P* high-*T* experiments were conducted by gradually increasing *T* to 400 °C
140 for siderite and to 500 °C for rhodochrosite at the same hardware conditions. A low flow
141 (~ 50 mL/min) of hydrogen-argon mixture gas (98 % Ar-2 % H₂) was introduced to
142 prevent the oxidation of divalent iron (Fe²⁺) and manganese (Mn²⁺) in the carbonates by
143 the air at high temperature.

144 The room-*T* (~ 20 °C) and high-*P* experiments were conducted up to 47 GPa in a
145 symmetrical anvil cell, equipped with type IIa diamond anvils with culet diameters of
146 500- or 250- μm . High-purity nitrogen gas (N₂, for experiments below 13 GPa) or helium
147 gas (He, for experiments above 13 GPa) at 160 MPa was loaded into the reaction
148 chamber as a pressure medium using high-pressure gas loading apparatus at the Center
149 for High Pressure Science and Technology Advanced Research (HPSTAR). Hydrostatic
150 conditions in the reaction chamber are expected to prevail over the full *P* range of our
151 experiments (Klotz et al. 2009). Siderite or rhodochrosite grains were loaded into a
152 pre-indented (80-30 μm thick) steel gasket, drilled with a 200-100 μm diameter hole. A

153 ruby sphere (BETSA) and small amount of $\text{SrB}_4\text{O}_7:\text{Sm}^{2+}$ grains (Zhao et al. 2017) were
154 loaded together with the carbonate samples as pressure sensors (Mao et al. 1986; Datchi
155 et al. 2007). The pressure deviation range given by ruby and $\text{SrB}_4\text{O}_7:\text{Sm}^{2+}$ was
156 consistently kept within ± 0.2 GPa in our experimental P - T range.

157 For the high P - T experiments, which were conducted up to 15 GPa and 1100 K for
158 siderite and up to 13 GPa and 900 K for rhodochrosite, we used a high- T BX-90 DAC.
159 Experiments were performed using ultra low-fluorescence type IIa diamonds with 500
160 μm culets. Heating was achieved using Ni-Cr wires wrapped around ZrO_2 seats that
161 support the diamond anvils. During operation, the whole cell was flushed with an Ar- H_2
162 mixture (98 % Ar-2 % H_2) to prevent the oxidation of the diamonds and Ni-Cr heaters by
163 air. An external cooling system was used to maintain the temperature of less than 100 $^\circ\text{C}$
164 in the body of the DAC while the sample was at high temperature for tens of hours. The
165 temperature was measured using K-type thermocouples attached to the diamond through
166 the heater wires, allowing the temperature of each diamond to be monitored during the
167 experiment (Fig. 1). Temperatures were calibrated based on the melting point of tin
168 (232 $^\circ\text{C}$), and the deviation was within 3 $^\circ\text{C}$. Rhenium gaskets with 80 μm thickness and
169 200 μm diameter holes were used to contain the sample, and a few pieces of $\text{SrB}_4\text{O}_7:$
170 Sm^{2+} were loaded into the sample chamber as the pressure sensor at high temperature
171 (Datchi et al. 2007). High-purity N_2 gas was used as a pressure medium.

172 In situ Raman measurements were performed using a confocal RM 1000 (Renishaw)
173 instrument equipped with a 532nm Nd: YAG laser, a Mitutoyo $\times 20$ long working
174 distance objective, and a grating with a groove density of 2400 grooves/mm at HPSTAR.
175 Each Raman spectrum was acquired between 100 cm^{-1} and 1250 cm^{-1} with a spectral
176 resolution of $\sim 1\text{ cm}^{-1}$ and acquisition time of 10 to 60 seconds. To obtain the steady-state
177 Raman frequency, measurements were carried out for 5 to 10 minutes following each
178 increase or decrease of P or T . All spectra were processed by PeakFit software (SeaSolve
179 software inc., Massachusetts, USA) and were calibrated against the measured excitation
180 of Si at $\sim 520\text{ cm}^{-1}$. After the baseline was subtracted with reasonable function, the
181 Raman peaks were fitted using symmetric Gauss + Lorentz function.

182

183

3. EXPERIMENTAL RESULTS

184 3.1 Atmospheric- P high- T experiments

185 Both siderite and rhodochrosite crystallize in the space group $R\bar{3}c$. The
186 rhombohedral carbonate minerals consist of two basic building blocks, the extremely
187 incompressible CO_3^{2-} groups (with an orientation of nearly planar CO_3^{2-} units, in which
188 the C-O bonds lie, perpendicular to z -axis), and the more compressible corner-linked
189 MO_6 octahedra (Redfern 2000; Farsang et al. 2020). Correspondingly, external Raman
190 modes (T and L mode) originate from the interactions between M^{2+} and CO_3^{2-} ions (M

191 represents Fe and Mn here), while ν_1 to ν_4 represent the internal modes of the CO_3^{2-}
192 group. The observed external modes (T, L) and internal modes of the CO_3^{2-} group (ν_1 , ν_4)
193 of both siderite and rhodochrosite are shown in Figure 2. The peaks of the Fe^{2+} electronic
194 excitation ($\sim 500 \text{ cm}^{-1}$), ν_4 ($\sim 730 \text{ cm}^{-1}$), and $2\nu_2$ overtone ($\sim 1720 \text{ cm}^{-1}$) modes of siderite,
195 as well as the ν_3 ($\sim 1400 \text{ cm}^{-1}$) and $2\nu_2$ overtone ($\sim 1720 \text{ cm}^{-1}$) modes of rhodochrosite, are
196 relatively weak or broad. Therefore, the peak positions determined by the Gauss +
197 Lorentz fitting are significantly imprecise and are not considered in this study. The
198 Raman frequency evolutions of siderite and rhodochrosite as a function of temperature
199 are reported in Figure 3, and the relative changes in frequency $\delta\nu_i/\delta T$ are compared with
200 literature data in Table 1. The frequencies of all measured modes decrease with increasing
201 temperature, and $\delta\nu_i/\delta T$ for the internal modes are generally less obvious than those of
202 the external modes. This behavior can be explained by the greater temperature sensitivity
203 of the M-O bond distance relative to that of the C-O bond (Gillet et al. 1993; Antao and
204 Hassan 2010), thus they displayed anisotropic thermal expansion. We find that a
205 nonlinear relationship between frequency shift and temperature fits our data best, whereas
206 Farsang et al. (2018, 2020) observed a linear $\delta\nu_i/\delta T$ relationship. However, our $\delta\nu_i/\delta T$
207 values for FeCO_3 are in good agreement with those of Liang et al. (2018) (Table 1). The
208 Raman shifts of FeCO_3 and MnCO_3 measured by Farsang et al. (2018) fluctuate greatly
209 with increasing temperature and they report poor goodness of fit statistics (R^2): 0.03 (T

210 mode), 0.87 (L mode), and 0.22 (ν_1 mode) for siderite and 0.98 (T mode), 0.99 (L mode),
211 0.13 (ν_4 mode), and 0.82 (ν_1 mode) for rhodochrosite. The poor fits of Farsang et al.
212 (2018) to $\delta\nu_i/\delta T$ data may indicate large temperature gradient in their heating stage,
213 which may be not calibrated well. Thermal decomposition of siderite was observed
214 between 350 and 400 °C, above which the vibrational modes cannot be detected. Raman
215 analysis and SEM-EDS characterization of the quenched products indicate that magnetite
216 and scaly graphite are produced. The decomposition T and products are in good
217 agreement with those in previous studies (Kissinger et al. 1956; Tao et al. 2013). Thermal
218 decomposition of rhodochrosite was observed between 400 and 425 °C, marked by the
219 sudden disappearance of all Raman bands. Only a broad Mn-O vibration ($\sim 650 \text{ cm}^{-1}$) can
220 be detected after quenching.

221 **3.2 Room T and high- P experiments**

222 The Raman mode frequency evolutions of siderite and rhodochrosite as a function of
223 pressure at room T are reported in Figure 4a and b, respectively. The relative changes in
224 frequency $\delta\nu_i/\delta P$ are listed in Table 1 in comparison with literature values. The
225 frequencies of all traced modes increase monotonously with P . Our $\delta\nu_i/\delta P$ values are in
226 good agreement with previous experiments of Farsang et al. (2018) at $P < 10$ GPa, which
227 were conducted under acceptable hydrostatic conditions when using a 4:1
228 methanol-ethanol fluid mixture (P_{max} of quasi-hydrostatic limit: < 9.8 GPa) as

229 pressure-transmitting medium (PTM). However, the $\delta v_i/\delta P$ values given by linear fitting
230 in other experimental studies (e.g., Farfan et al. 2012; Cerantola et al. 2015; Liang et al.
231 2018; Farfan et al. 2013; Zhao et al. 2018) over a wider P range are generally lower than
232 our studies (Table 1). These differences cannot be attributed to compositional effects, as
233 our materials have almost identical compositions to those in other studies. One possible
234 explanation is the development of a non-hydrostatic stress regime in the DAC
235 experiments from previous studies because their experimental pressure more or less
236 exceeds the hydrostatic limits of pressure mediums of the silicon oil, neon, and nitrogen
237 at ~ 2 , ~ 16 , and ~ 13 GPa, respectively (Klotz et al. 2009). Another possible explanation is
238 that the linear fit is not adapted to the data under high pressure. For instance, Liu et al.
239 (2016) used helium as pressure medium, which is considered be able to produce
240 hydrostatic conditions at above 50 GPa, but they calculated a smaller $\delta v_i/\delta P$ value for
241 MnCO_3 in comparison with that from our study. A subset of 0-47 GPa high-pressure
242 experiments (see section below) show a linear relationship for carbonate modes between
243 the peak position and pressure at ≤ 10 GPa, whereas a nonlinear relationship is observed
244 at higher P above 10 GPa. Nonlinear $\delta v_i/\delta P$ trends are observed for MnCO_3 in
245 comparison with FeCO_3 . Based on this, we further explored the relationship between
246 $\delta v_i/\delta P$ and the fitting pressure range, as shown in the Supplementary Figure OM1. For
247 FeCO_3 , our results show that as the fitting range becomes larger, $\delta v_i/\delta P$ systematically

248 decreases. If assuming a linear relationship between the peak position and pressure, our
249 $\delta v_i/\delta P$ values are very close to Cerantola et al. (2015) (3.80 vs. 3.82 for L mode; 2.13 vs.
250 2.17 for v_1 mode) in the similar fitting range (0-45 GPa vs. 0-40 GPa). For MnCO_3 , a
251 larger fitting range also lowers the $\delta v_i/\delta P$ values. If assuming a linear relationship
252 between the peak position and pressure, our $\delta v_i/\delta P$ values are very close to Liu et al.
253 (2016) (2.95 vs. 2.91 for T mode; 1.38 vs. 1.28 for v_4 mode; 2.13 vs. 2.17 for v_1 mode) in
254 the same fitting range (0-45 GPa). When Farfan et al. (2013) and Zhao et al. (2018)
255 reported a transition of MnCO_3 between 15 and 35 GPa, $\delta v_i/\delta P$ values of MnCO_3 -I will
256 fluctuate greatly and deviate from the trend. The problem of the incorrect application of
257 linear fitting algorithms may also be compounded if a non-hydrostatic PTM is used,
258 resulting in differential and shear stresses that will also affect the $\delta v_i/\delta P$ values.

259 For both the FeCO_3 and MnCO_3 , the lowest $\delta v_i/\delta P$ is observed for internal modes
260 (v_1 or v_4) and the highest $\delta v_i/\delta P$ is observed for the T mode, displaying anisotropic
261 compression (Fig. 4, Table 1), because the compressibility along the z crystallographic
262 axis (in the hexagonal setting) is much larger than along the x -axis (Zhang and Reeder
263 1999; Redfern 2000; Wang et al. 2018; Farsang et al. 2020). As a result, $\delta v_i/\delta P$ values of
264 the external lattice mode (T, L) are more sensitive to pressure in comparison with the
265 internal modes of the CO_3^{2-} unit, where the C-O bonds lie perpendicular to the z -axis.
266 Additionally, although MnCO_3 and FeCO_3 are isostructural solids, carbonates with large

267 cations (e.g., Mn^{2+} (0.83 Å) vs. Fe^{2+} (0.78 Å)) exhibit a larger positive $\delta\nu_i/\delta P$ for ν_1 and
268 ν_4 , indicating a more significant MO_6 octahedral distortion (Farsang et al. 2020).

269 **3.3 High- T and high- P experiments**

270 For the first time, we report the Raman vibrational behavior of MnCO_3 and FeCO_3
271 at high- T and high- P , simultaneously. Several sets of high- T and high- P experiments
272 were carried out systematically, and the coupled effect of P and T on Raman shift is
273 presented in Figure 5. A polynomial expression was fitted to the curved surface of Raman
274 frequency shift data across the full experimental P - T range and the following equations
275 were derived:

276 For siderite (FeCO_3):

277 (1) T mode

$$278 \quad \nu(P, T) = 183.163 - 0.00977 \times T + 4.243 \times P + 4.172 \times 10^{-6} \times T^2 - 0.08425 \times P^2 \\ + 8.288 \times 10^{-4} \times P \cdot T \quad (R^2 = 0.998)$$

279 (2) L mode:

$$280 \quad \nu(P, T) = 283.535 - 0.01223 \times T + 5.041 \times P - 1.717 \times 10^{-6} \times T^2 - 0.05777 \times P^2 \\ + 2.672 \times 10^{-4} \times P \cdot T \quad (R^2 = 0.998)$$

281 (3) ν_1 mode:

$$282 \quad \nu(P, T) = 1085.505 - 0.00643 \times T + 3.056 \times P - 2.853 \times 10^{-6} \times T^2 - 0.0734 \times P^2 \\ + 5.998 \times 10^{-4} \times P \cdot T \quad (R^2 = 0.994)$$

283

284 For rhodochrosite (MnCO_3):

285 (4) T mode:

286
$$\nu(P, T) = 185.6075 - 0.0257 \times T + 3.8149 \times P + 8.1999 \times 10^{-6} \times T^2 - 0.0537 \times P^2$$
$$+ 9.8688 \times 10^{-4} \times P \cdot T \quad (R^2 = 0.998)$$

287 (5) L mode:

288
$$\nu(P, T) = 290.1466 - 0.0321 \times T + 5.6446 \times P + 4.0518 \times 10^{-6} \times T^2 - 0.1092 \times P^2$$
$$+ 1.63 \times 10^{-3} \times P \cdot T \quad (R^2 = 0.999)$$

289 (6) ν_4 mode:

290
$$\nu(P, T) = 719.5914 - 0.0059 \times T + 2.3374 \times P + 2.1554 \times 10^{-6} \times T^2 - 0.0585 \times P^2$$
$$+ 3.92 \times 10^{-4} \times P \cdot T \quad (R^2 = 0.995)$$

291 (7) ν_1 mode:

292
$$\nu(P, T) = 1085.9578 - 0.0082 \times T + 3.8162 \times P - 2.7963 \times 10^{-6} \times T^2 - 0.0726 \times P^2$$
$$+ 6.8004 \times 10^{-4} \times P \cdot T \quad (R^2 = 0.999)$$

293

294 Equations (1~7) show that the frequency shifts of the different carbonate modes are
295 a coupled function of both P and T . The shifts obtained by summing expressions for
296 $(\delta\nu_i/\delta T)_P$ (equations in Fig. 3) and $(\delta\nu_i/\delta P)_T$ (equations in Fig. 4) increasingly deviate
297 from the measured data: The predicted frequency shift of the L mode is off by 4.5 cm^{-1}
298 and 5.5 cm^{-1} at the highest P - T conditions for siderite and rhodochrosite, respectively, and
299 are outside the analytical uncertainty. Therefore, the P - T cross derivative term cannot be
300 neglected at high P - T conditions, which has been done in previous studies (e.g., Facq et
301 al. 2014, 2016; Farsang et al. 2018; see more detail in below section).

302

303

4. DISCUSSION

304 4.1 Calculation of the mode Grüneisen and intrinsic anharmonic parameters

305 Pressure-induced frequency shifts of a vibrational mode are the result of the volume
306 change due to compressibility, whereas T -induced frequency shifts arise from both
307 volume changes due to thermal expansion and phonon-phonon interactions (Gillet et al.
308 1989, 1998; Farsang et al. 2020). The mode Grüneisen parameter (γ_i) describes the
309 relative contributions of each vibration to the thermochemical properties (Anderson 2000;
310 Liang et al. 2018). The deviation of vibrational frequency (ν_i) as a function of volume (V)
311 represents the mode Grüneisen parameter for a phonon mode following the relation (Born
312 and Huang 1954):

313

$$\gamma_i = -\frac{\partial \ln \nu_i}{\partial \ln V} \quad (8)$$

314

315 The mode Grüneisen parameters (γ_{iT} , γ_{iP}) describe the P and T dependence at the
316 isothermal and isobaric conditions of the vibrational mode, respectively, and are
expressed as:

317

$$\begin{aligned} \gamma_{iT} &= -\frac{K_T \partial \nu_i}{\nu_{i0} \partial P}, \\ \gamma_{iP} &= -\frac{\partial \nu_i}{\alpha_T \nu_{i0} \partial T} \end{aligned} \quad (9a, 9b)$$

318 Where K_T is the isothermal bulk modulus, α_T is the isobaric thermal expansion coefficient,
319 ν_{i0} is each vibration frequency at corresponding isothermal or isobaric conditions, and

320 $\partial v_i/\partial P$ or $\partial v_i/\partial T$ is the partial derivatives of the frequency shift as a function of P and
321 fixed T , or T and fixed P .

322 Gillet et al. (1989) have used a mode anharmonic parameter (a_i) for considering
323 crystal anharmonicity, which expresses the change in frequency due to T at constant
324 volume:

$$325 \quad a_i = \left(\frac{\partial \ln v_i}{\partial T} \right)_v = \alpha(\gamma_{iT} - \gamma_{iP}) \quad (10)$$

326 In the pure harmonic approximation $a_i = \gamma_{iT} = \gamma_{iP} = 0$. Here, we calculated the
327 isobaric and isothermal equivalents of the Grüneisen parameter and the anharmonic
328 parameter for siderite and rhodochrosite (Tables 2 and 3). We used K_0 and α_0 to calculate
329 γ_{iT} and γ_{iP} at 20 °C, 1 bar respectively. The values of the γ_{iT} , γ_{iP} , and a_i span a much larger
330 range for the external lattice modes (T, L) than the internal modes (v_4 , v_1) in both FeCO₃
331 and MnCO₃. Therefore, anisotropic compression (Zhang and Reeder 1999; Redfern 2000;
332 Liang et al. 2018; Farsang et al. 2018, 2020) and anisotropic thermal expansion (Wang et
333 al. 2018; Farsang et al. 2018, 2020) exist. The external modes are expected to contribute
334 significantly more to the intrinsic anharmonicity, and may also be reflected in the $\delta v_i/\delta T$
335 and $\delta v_i/\delta P$ values discussed above. Both the thermal expansion and compression of
336 FeCO₃ and MnCO₃ along the z crystallographic axis are much larger than that along the x
337 axis (Zhang and Reeder 1999; Redfern 2000; Wang et al., 2018; Farsang et al., 2020). For
338 FeCO₃, our γ_{iT} values are very close to the results in Farsang et al. (2018), but larger than

339 those reported by Cerantola et al. (2015) and Liang et al. (2018) (Table 2), which may
340 underestimate the value of $\delta v_i/\delta P$ due to the non-hydrostatic effect or inappropriate use of
341 a linear fit over a wide pressure range. The γ_{iP} values reported by Farsang et al. (2018) for
342 FeCO_3 are significantly different with that from our study. However, these differences are
343 the result of poorly resolved $\delta v_i/\delta T$ data in Farsang et al. (2018), so that a_i also has a
344 deviation. For MnCO_3 , our γ_{iT} values and those of Farsang et al. (2018) and Liu et al.
345 (2016) are in close agreement, consistent with the hydrostatic conditions in these
346 experiments, However, the data of Zhao et al. (2018) are not in agreement (Table 3). The
347 γ_{iP} is different due to the selection of α_0 values, but overall, our results are more similar to
348 Zhao et al. (2018), at least we report γ_{iP} values with the same (positive) sign.

349 The a_i , γ_{iT} and γ_{iP} parameters are T -dependent because K_T , α , and v_i are known
350 functions of temperature (except for K_T of MnCO_3). Thus, we can examine the variation
351 of a_i with temperature and calculate the propagated uncertainty in a_i (Gillet et al. 1990).
352 Here, $\gamma_{iT(300)}$, $\gamma_{iP(300)}$ and $a_{i(300)}$ for siderite are calculated using values of v_i , K_T and α_T at
353 300°C by assuming $\delta v_i/\delta P$ to be independent of T , so is rhodochrosite (Tables 2 and 3).
354 For FeCO_3 , the γ_{iT} and γ_{iP} of all modes decrease with T , and the a_i parameter increases
355 between 20 and 300°C. For MnCO_3 , the γ_{iT} and γ_{iP} of external lattice modes (T, L)
356 increase slightly with increasing T , whereas the internal modes (v_4 , v_1) are relatively

357 constant from 20 °C to 250 °C. Overall, the P - T cross term becomes important for
358 mineral behavior if both P and T are elevated.

359 **4.2 Calculation of the bulk modulus parameters**

360 To date there is no treatment of the temperature dependence of the bulk modulus for
361 MnCO_3 . We developed a method of using high P - T Raman scattering data to calculate the
362 mode (macroscopic) Grüneisen parameters (γ_i) and the bulk modulus parameter (K_T), as
363 long as K_0 is known from a fit of isothermal (room T condition) compression XRD data.
364 In situ high- P and high- T Raman experiments are relatively simple to implement in
365 comparison with XRD measurements under the same conditions, and our approach may
366 thus have broad use to the community. Here, we highlight our approach and evaluate its
367 effectiveness. We use a first-order Murnaghan equation of state (Murnaghan 1937)
368 expressed in terms of the Raman frequency (Datchi et al. 2004):

$$369 \quad \nu_i(P, 20^\circ\text{C}) = \nu_i(1 \text{ bar}, 20^\circ\text{C}) \left(1 + \frac{K'}{K_0} P\right)^{\gamma_i/K'} \quad (11)$$

370 Using the bulk modulus K_0 (117 GPa for siderite; 110 GPa for rhodochrosite) and
371 fixed its first derivative $K_0' = 4$, a least-squares fit of Eq. 11 to our high- P Raman data at
372 ambient temperature allows us to determine $\nu_i(1 \text{ bar}, 20^\circ\text{C})$ and γ_{iT} (Table 4). The fits to
373 our data produce R^2 values close to 1, and the derived parameters (ν_i, γ_{iT}) are consistent
374 with the measured/calculated values presented in earlier sections. To extract values for K_T
375 from the present simultaneously high P - T measurements, we assumed that the change in

376 K_0' with temperature is negligible and that K_T can be approximated by a linear function.

377 Therefore, Eq. 11 can be generalized in the form

378
$$v_i(P, T) = v_i(1 \text{ bar}, T) \left(1 + \frac{K'}{K_T} P\right)^{\gamma_i/K'} \quad (12)$$

379 where $v_i(1 \text{ bar}, T)$ is shown in Figure 3. By fitting K_T to the whole Raman data set (0-15

380 GPa, 20-800 °C for siderite; 0-13 GPa, 20-600 °C for rhodochrosite) of the highest

381 intensity $\nu_1 A_{1g}$ symmetric C-O stretching mode, we obtained

382
$$\begin{aligned} K_T(\text{FeCO}_3) &= 117 - 0.02961 \times (T - 20); \\ K_T(\text{MnCO}_3) &= 110 - 0.01735 \times (T - 20) \end{aligned} \quad (13a, 13b)$$

383 Where T is in °C, and the derived mode macroscopic Grüneisen parameters (γ_i) and fitting

384 R^2 are reported in Table 4. While we observed that the macroscopic γ_i exhibits some

385 scattering at high P - T conditions relative to ambient conditions, these variations do not

386 propagate to significant uncertainties in our fitting results. Zhang et al. (1998) obtained

387 the T -dependence of the bulk modulus K_T of siderite ($\text{Fe}_{0.998}\text{Mn}_{0.002}\text{CO}_3$) by in situ X-ray

388 diffraction at conditions up to 8.9 GPa and 800 °C. We have evaluated the difference

389 between our derived K_T and Zhang et al. (1998) (Table. 4), and the results show that even

390 at temperatures as high as 773 K, the deviation of the prediction is only 0.5 GPa. This

391 comparison demonstrates the accuracy and reasonability of our prediction model (Eqs. 11

392 to 13) based on the Murnaghan equation of state. Therefore, it is likely that there are no

393 large systematic errors associated with our estimate of K_T for rhodochrosite, and Equation
394 13b may be applied accurately within the T range of 20 to 600 °C.

395 **4.3 Development of a P - T calibrant**

396 Subduction of carbonates is a key process for the Earth's long-term deep carbon
397 cycle. Numerical high-pressure experiments based on DAC technology and in situ Raman
398 spectroscopy measurements have been applied to studying solubility of carbonate in
399 aqueous fluids (e.g., Facq et al. 2014, 2016), water-rock reaction (e.g., Scott et al. 2004;
400 Chen et al. 2008), and in other areas. However, accurate determination of in situ pressure
401 in the reaction chamber of DAC in high- T (> 400 °C) aqueous systems has been
402 hampered in this area. Pressure sensors commonly used for calibration are known to
403 result in contamination of the studied aqueous system. For example, ruby, a
404 Cr^{3+} -containing $\alpha\text{-Al}_2\text{O}_3$ phase, gradually dissolves in aqueous fluids during heating
405 (Tropper and Manning 2007; Andreani et al. 2013). Additionally, the broadening of the
406 ruby R_1 and R_2 fluorescence peaks at high- T decreases the signal-to-background ratio of
407 the Raman bands and results in uncertainties for pressure determination (Goncharov et al.
408 2005; Datchi et al. 2007; Farsang et al. 2018). Other pressure sensors, such as SrB_4O_7 :
409 Sm^{2+} , quartz, and zircon, also exhibited increased solubility at high- T (Manning 1994;
410 Datchi et al. 2007; Bernini et al. 2013). Although ^{13}C diamond is a potential candidate
411 material for the study of C-H-O aqueous systems, the Raman shift is relatively

412 P -insensitive ($2.83 \text{ cm}^{-1}/\text{GPa}$, Schiferl et al. 1997). Here, we used our Raman data to
413 develop P - T calibrants for siderite and rhodochrosite. These calibrants will be particularly
414 useful for carbonate solubility and water-carbonate reaction for DAC experiments as no
415 adverse chemical interactions between the sample and the pressure sensor or pressure
416 transmitting medium (PTM) are expected. Facq et al. (2014, 2016) and Farsang et al.
417 (2018) first attempt to establish carbonate pressure sensors using linearly superimposed
418 independent P - and T -induced shifts of carbonate modes but ignored the P - T cross
419 derivative term of the frequency. Here, we considered the cross-derivative term in our
420 treatment of P estimation by inverting Eqs. (1 to 7):

$$421 \quad P = \frac{-B(T) + \sqrt{B(T)^2 - 4A \cdot (C(T) - v_i(P, T))}}{2A} \quad (14)$$

422 Where A , B , and C are calculated as for siderite (FeCO_3):

423 (15) T mode:

$$424 \quad A = -0.08425; B(T) = 4.243 + 8.288 \times 10^{-4} \cdot T; C(T) = 183.163 - 0.00977 \cdot T + 4.172 \times 10^{-6} \cdot T^2$$

425 (16) L mode:

$$426 \quad A = -0.05777; B(T) = 5.041 + 2.672 \times 10^{-4} \cdot T; C(T) = 283.535 - 0.01223 \cdot T - 1.717 \times 10^{-6} \cdot T^2$$

427 (17) ν_1 mode:

$$428 \quad A = -0.0734; B(T) = 3.056 + 5.998 \times 10^{-4} \cdot T; C(T) = 1085.505 - 0.00643 \cdot T - 2.853 \times 10^{-6} \cdot T^2$$

429

430 And for rhodochrosite (MnCO_3):

431 (18) T mode:

432 $A = -0.0537; B(T) = 3.8149 + 9.8688 \times 10^{-4} \cdot T; C(T) = 185.6075 - 0.0257 \cdot T + 8.1999 \times 10^{-6} \cdot T^2$

433 (19) L mode:

434 $A = -0.1092; B(T) = 5.6446 + 1.63 \times 10^{-3} \cdot T; C(T) = 290.1466 - 0.0321 \cdot T + 4.0518 \times 10^{-6} \cdot T^2$

435 (20) ν_4 mode:

436 $A = -0.0585; B(T) = 2.3374 + 3.92 \times 10^{-4} \cdot T; C(T) = 719.5914 - 0.0059 \cdot T + 2.1554 \times 10^{-6} \cdot T^2$

437 (21) ν_1 mode:

438 $A = -0.0726; B(T) = 3.8162 + 6.8004 \times 10^{-4} \cdot T; C(T) = 1085.9578 - 0.0082 \cdot T - 2.7963 \times 10^{-6} \cdot T^2$

439

440 The above equations can be used to determine the in-situ P based on the Raman shift
441 and T measured by the thermocouple during high-temperature DAC experiments (e.g.,
442 Figs. 5c and 5d). In Figure 6 we compared the difference in predicted pressures with and
443 without accounting for the P - T cross term effects. Without considering the cross term, the
444 calculated P may deviate from the real pressure by as much as ~ 0.5 GPa for FeCO_3 and
445 ~ 2 GPa for MnCO_3 . For FeCO_3 , the largest deviations occur at low- T and high- P ,
446 whereas the largest deviations for MnCO_3 are at high- T . These data demonstrate that the
447 influence of the P - T cross term on the predicted P is significantly greater for MnCO_3
448 compared to FeCO_3 .

449 It is well known that empirical polynomial fits, like Eq. 14, result in poor
450 extrapolations outside of their calibration range. Instead, Eq. 12 is grounded in the
451 physical relationship between the bulk modulus and pressure and is likely to be more
452 accurate outside of the calibrated P - T range. We inverted Eq. 12 to solve for P as a
453 function of T and the measured Raman frequency:

$$454 \quad P_{FeCO_3} = \left[29.25 - 7.4 \times 10^{-3} \cdot (T - 20) \right] \cdot \left\{ \left[\frac{v_1(P, T)}{v_1(0, T)} \right]^{12.90} - 1 \right\}; \quad (22a, 22b)$$
$$P_{MnCO_3} = \left[27.50 - 4.35 \times 10^{-3} \cdot (T - 20) \right] \cdot \left\{ \left[\frac{v_1(P, T)}{v_1(0, T)} \right]^{10.53} - 1 \right\}$$

455 To use equations 14 and 22, it is necessary to evaluate (1) the most suitable modes
456 for P - T determination and (2) the range of P - T conditions over which these equations
457 may be applied accurately. The difference between the measured real pressures and
458 pressures calculated with various modes using Eq. 14 or Eq. 22 is shown in
459 supplementary Figs. OM2 and OM3. We find that predictions based on L and v_1 modes
460 with Eq. 14 are nearly identical and match the known P of the experiments within ± 0.25
461 GPa (even smaller). However, the pressure calculated by Eq. 22 has a large deviation
462 from the actual at low pressure, and gradually drops back under high pressure, which
463 means that the Eq. 22 derived from Murnaghan equation of state may have better
464 high-pressure epitaxy for both siderite and rhodochrosite (Supplementary Figs. OM2a, 2d,
465 3a and 3d). Therefore, we recommend the use of Eq. 14 for calculations of P within our

466 *P-T* calibration range from in situ Raman spectral measurements of FeCO₃ and MnCO₃,
467 whereas Eq. 22 may be suitable for calculations at > 15 GPa (outside our calibration
468 range). Additionally, we find that the different Raman-active vibrational modes exhibit
469 different degrees of intensity and *P*, *T* sensitivity, affecting their predictive power
470 (Supplementary Figs. OM2b, 2c, 3b, 3c, 3d and 3e). We find that the L mode, ν_1 mode, T
471 mode, and ν_4 mode (in decreasing order) are the most suitable for *P* determination (see
472 Table 1). The signal intensity at low wavenumbers (less than 150 cm⁻¹) for the Raman
473 instrument used in this study is relatively low, which significantly limits our ability to
474 consistently fit the T mode data. In addition, the peak intensity of ν_4 is much lower than
475 that of the L and ν_1 modes, resulting in poor fitting statistics. While the ν_1 and L modes
476 are both at high intensities, we find that the peak position of the L mode is more sensitive
477 to changes in *P-T*. Taken together, we recommend the above sequence.

478 **4.4 Phase transitions of siderite and rhodochrosite at high *P* and room *T***

479 We also examined the potential phase changes, spin transitions, and structural
480 changes in FeCO₃ and MnCO₃ as a function of *P* up to 47 GPa at room *T* to explore the
481 applicable scope of the thermodynamic parameters/behaviors obtained above, to some
482 degree. The Raman spectra of FeCO₃ demonstrate that it is stable up to ~ 44 GPa at
483 ambient temperature (Fig. 7a). However, we observed that the intensities of T, L, and ν_4
484 modes gradually decrease (Supplementary Material Fig. OM4a). Between 43.6 and 46.6

485 GPa, we observed an obvious frequency change in all modes, which is a consequence of
486 the spin transition. Both of the external lattice modes (L and T modes) and the internal
487 mode (ν_4) jump to higher wavenumbers as the distance between the CO_3^{2-} groups and the
488 cations, as well as the O-O bond lengths, decrease, respectively (Farfan et al. 2012; Lin et
489 al. 2012; Cerantola et al. 2015; Müller et al. 2016). Contrary to the other modes, the ν_1
490 mode is shifted to lower wavenumbers as the result of an increase of C-O bond lengths
491 after the spin transition (Lavina et al. 2010). The color of the crystal also changes from
492 transparent to green at the same time as the phase changes (Fig. 7a). The *P*-induced,
493 isostructural high-spin (HS) to low-spin (LS) transition is caused by the increase in the
494 crystal field splitting energy of the 3d electrons of Fe^{2+} in its octahedrally-coordinated
495 site under compression (Farfan et al. 2012). The transition results in a decrease in volume
496 and octahedral bond distance, an increase in bulk modulus, and a slight increase in the
497 C-O bond length of the CO_3^{2-} groups (Lavina et al. 2009, 2010; Nagai et al. 2010). The *P*
498 of the HS to LS transitions reported in previous literature are summarized in Table 5.
499 Depending on the experimental methods, a general inconsistency about the pressure
500 range of the spin transition exists. Our results support the viewpoint of a sharp spin
501 transition (a range of ≤ 3 GPa), whereas some studies (e.g., Spivak et al. 2014; Cerantola
502 et al. 2015) place the spin transition over a sizeable pressure range (≥ 5 GPa).
503 Interestingly, even when more magnesium-bearing siderite is used (e.g., $\text{Fe}/(\text{Fe}+\text{Mg}) =$

504 0.65), the transition pressure still occurs in the vicinity of 45 GPa. The negligible
505 compositional effect on the transition pressure in the (Mg, Fe)CO₃ system can be
506 explained by the much longer Fe²⁺-Fe²⁺ distances in the structure that are separated by
507 the CO₃²⁻ units (Lin et al. 2012).

508 The Raman frequency shift of MnCO₃ as a function of *P* at room *T* is shown in
509 Figure 7b and Supplementary Material Figure OM4b. Like siderite, the intensities of T, L,
510 and *v*₄ modes of rhodochrosite gradually decrease with increasing *P*. In the compression
511 data, we observed an abrupt step in the Raman shift of the *v*₁ mode at 46.6 GPa, where a
512 new, higher frequency peak forms and the intensity of the original peak is diminished
513 (Supplementary Material Fig. OM4b), which we assign to the change from MnCO₃-I
514 (CaCO₃-I type structure) to MnCO₃-II (CaCO₃-VI type structure) (Merlin et al. 2015; Liu
515 et al. 2016). The L, T, and *v*₄ modes are split, and the splitting of the *v*₄ modes occurs at a
516 higher wavenumber than the initial peak. Other new peaks may exist but are difficult to
517 identify due to the weak intensity or overlap. Our results closely resemble those of Liu et
518 al. (2016) and Merlini et al. (2015) on the MnCO₃-I to MnCO₃-II transition (Table 5),
519 where the structural state of MnCO₃ was measured by XRD and Raman spectroscopy and
520 helium was used as a PTM. However, our results differ from those of other studies. For
521 example, Farfan et al. (2013), Boulard et al. (2015) and Zhao et al. (2018) reported a
522 transition of MnCO₃ between 15 and 35 GPa using NaCl, silicon oil or N₂ as the

523 pressure-transmitting medium and that this transition may be related to a distortion of the
524 CaCO_3 -I structure due to nonhydrostatic conditions, especially when NaCl undergoes a
525 B1 to B2 phase transition about 25-30 GPa, which involves a fairly large volume change
526 (Liu et al. 2016). Meanwhile, Ono (2007) did not observe this distorted phase after laser
527 heating, which removed the non-hydrostatic effect and could be considered as a
528 hydrostatic pressure environment. But this study lacks experiments between 44 and 54
529 GPa, only roughly estimated that MnCO_3 would undergo a phase transition at ~ 50 GPa.
530 Santillan and Williams (2004) did not observe any phase transition up to 50 GPa, which
531 may be related to the relatively impure composition of their sample
532 ($\text{Mn}_{0.77}\text{Fe}_{0.09}\text{Ca}_{0.07}\text{Mg}_{0.07}\text{CO}_3$). The incorporation of Fe^{2+} and Mg^{2+} in MnCO_3 sample
533 may enlarge the stability field of the CaCO_3 -I structure of MnCO_3 (Shi et al. 2012;
534 Boulard et al. 2015; Liu et al. 2016). In short, we find that the transition pressures
535 obtained by XRD and Raman using helium as the PTM are consistent (Table 5). Helium
536 is considered the best hydrostatic pressure media, with a pressure difference of less than
537 0.5 GPa at 50 GPa (Klotz et al. 2009). Furthermore, no coexisting MnCO_3 -I and
538 MnCO_3 -II phases (the distorted phase of the CaCO_3 -I structure) are observed between 15
539 and 35 GPa. As emphasized previously, the choice of PTM is crucial to maintaining
540 hydrostatic conditions in DAC experiments. In addition, the large difference of phase
541 transition pressure for MnCO_3 under non-hydrostatic and hydrostatic conditions indicates

542 that it may be different from other carbonates, which seems sensitive to the stress field in
543 the sample chambers (Liu et al. 2016; Zhao et al. 2018).

544 Previous studies have concluded that the observed jumps in the Raman spectra for
545 MnCO_3 are the result of changes in the crystal structure itself, with no contribution of an
546 electronic spin transition of Mn^{2+} (Farfan et al. 2013; Boulard et al. 2015). As a result, the
547 bulk modulus and density of MnCO_3 increase by approximately 12 % and 5.5 % across
548 the phase transition from I to II (Liu et al. 2016). These data suggest that although the Ca,
549 Mg, Fe, and Mn carbonate group minerals all have the same structure at ambient
550 conditions (rhombohedral, space group $R\bar{3}c$), their high-pressure behavior is markedly
551 different due to the size, charge, or electronic configuration of their constituent atoms
552 (Zhang and Reeder 1999).

553

554 **5. IMPLICATIONS**

555 To date, little is known about the fate of the FeCO_3 and MnCO_3 carbonates in the
556 subduction zones and Earth's deep interior. These components may be significant:
557 MnCO_3 is found as a vein-filling phase in seafloor hydrothermal ore deposits (Hazen et al.
558 2013) and the FeCO_3 component is present as a solid solution of magnesite and dolomite
559 in metamorphosed iron formations (Klein 1978, 2005), altered igneous rocks (Buckley
560 and Woolley 1990; Laverne 1993), and so on. To address this knowledge gap, we

561 systematically quantified the effects of temperature, pressure, and the P - T cross
562 derivative on the Raman frequency shifts of siderite and rhodochrosite. Additionally, we
563 report the first (to our knowledge) measurements of the Raman spectra of these phases at
564 simultaneously high- P and high- T conditions, which we analyzed over the range 0 to 15
565 GPa and 300 to 1100 K. Importantly, we used these data to develop Raman shift pressure
566 sensors of siderite and rhodochrosite. Particularly because other commonly used pressure
567 calibrants (e.g., ruby, $\text{SrB}_4\text{O}_7: \text{Sm}^{2+}$, quartz) in the sample chamber are known to change
568 the reaction system due to their instability at high P - T conditions, especially involving
569 aqueous systems. The derived temperature from 300 to 1100 K at high pressure up to 15
570 GPa in our study covers a significant portion of the P - T range for the subduction zones.
571 The v_i - P - T relationships of siderite and rhodochrosite established in our study can be
572 used specifically to calibrate pressure of the reaction chamber while studying the
573 solubility of FeCO_3 and MnCO_3 in water or the water-carbonate interaction progress (e.g.,
574 in Fe-C-O-H or Mn-C-O-H system) under the conditions of the deep Earth, so as to
575 derive important physical and chemical properties. More research is needed to reveal
576 carbon behavior in aqueous-bearing systems in the subduction zones.

577 Additionally, the measured P -, T -, and P - T cross induced Raman frequency shifts
578 were used to calculate the mode Grüneisen, intrinsic anharmonic and bulk modulus
579 parameters. We developed a method based on a first-order Murnaghan equation of state

580 to calculate the temperature dependence of the bulk modulus (K_T), which is more
581 convenient and low-cost than in situ high- P and high- T XRD measurements. The derived
582 anharmonic thermodynamic properties allow us to refine the phase diagram for FeCO_3
583 and MnCO_3 systems at high P - T conditions.

584 Finally, we re-examined the high- P phase transition behavior of siderite and
585 rhodochrosite at room temperature. A sharp spin transition in FeCO_3 is observed at ~ 45
586 GPa, and the transition of MnCO_3 -I to MnCO_3 -II occurs at ≥ 46 GPa. Further
587 simultaneous high- P and high- T experiments relevant to subduction zones will be needed
588 to quantify the phase transition boundaries for divalent carbonates. Such data are vital to
589 constrain the fate of carbonates in subduction zones and the deep carbon cycle behaviors.

590

591

ACKNOWLEDGMENTS

592 This study was supported by the National Key Research and Development Program
593 of China (2019YFA0708501) and the NSFC Major Research Plan on West-Pacific Earth
594 System Multispheric Interactions (project number: 92158206). Many thanks to Dr.
595 Chaoshuai Zhao for kindly providing the synthetic $\text{SrB}_4\text{O}_7: \text{Sm}^{2+}$, and Dr. Freyja O'Toole
596 for editing English. We also thank two anonymous reviewers for their constructive
597 comments and Dr. Bin Chen (Associate Editor) for his careful editorial handling and
598 helpful suggestions.

599

600

REFERENCES CITED

601 Anderson, O.L. (2000) The Grüneisen ratio for the last 30 years. *Geophysical Journal*

602 *International*, 143, 279–294.

603 Andreani, M., Daniel, I., and Pollet-Villard, M. (2013) Aluminum speeds up the

604 hydrothermal alteration of olivine. *American Mineralogist*, 98, 1738–1744.

605 Anovitz, L.M., and Essene, E.J. (1987) Phase equilibria in the system

606 $\text{CaCO}_3\text{-MgCO}_3\text{-FeCO}_3$. *Journal of Petrology*, 28, 389–415.

607 Antao, S.M., and Hassan, I. (2010) Temperature dependence of the structural parameters

608 in the transformation of aragonite to calcite, as determined from in situ synchrotron

609 powder X-ray-diffraction data. *Canadian Mineralogist*, 48, 1225–1236

610 Bernini, D., Audétat, A., Dolejš, D., and Keppler, H. (2013) Zircon solubility in aqueous

611 fluids at high temperatures and pressures. *Geochimica et Cosmochimica Acta*, 119,

612 178–187.

613 Born, M., and Huang, K. (1954) *Dynamical theory of crystal lattices*. Oxford University

614 Press, U.K.

615 Boulard, E., A. F. Goncharov, M. Blanchard, and W. L. Mao (2015), Pressure-induced

616 phase transition in MnCO_3 and its implications on the deep carbon cycle. *Journal of*

617 *Geophysical Research: Solid Earth*, 120, 4069–4079.

- 618 Buckley, H.A., and Woolley, A.R. (1990) Carbonates of the magnesite–siderite series
619 from four carbonatite complexes. *Mineralogical Magazine*, 54, 413–418.
- 620 Cerantola, V., Bykova, E., Kuppenko, I., Merlini, M., Ismailova, L., McCammon, C., and
621 others. (2017) Stability of iron-bearing carbonates in the deep Earth’s interior.
622 *Nature Communications*, 8, 15960–15960.
- 623 Cerantola, V., McCammon, C., Kuppenko, I., Kantor, I., Marini, C., Wilke, M., Ismailova,
624 L., Solopova, N., Chumakov, A., Pascarelli, S., and others. (2015) High-pressure
625 spectroscopic study of siderite (FeCO₃) with a focus on spin crossover. *American*
626 *Mineralogist*, 100, 2670–2681.
- 627 Chen, J.Y., Jin, L.J., Dong, J.P., Zheng, H.F., and Liu, G.Y. (2008) Methane formation
628 from CaCO₃ reduction catalyzed by high pressure. *Chinese Chemical Letters*, 19,
629 475–478.
- 630 Dasgupta, R. and Hirschmann, M.M. (2010) The deep carbon cycle and melting in
631 Earth’s interior. *Earth and Planetary Science Letters*, 298, 1–13.
- 632 Dasgupta, R., and Hirschmann, M.M. (2006) Melting in the Earth’s deep upper mantle
633 caused by carbon dioxide. *Nature*, 440, 659–662.
- 634 Datchi, F., and Canny, B. (2004) Raman spectrum of cubic boron nitride at high pressure
635 and temperature. *Physical Review B*, 69, 144106.
- 636 Datchi, F., Dewaele, A., Loubeyre, P., Letoulliec, R., Le Godec, Y., and Canny, B. (2007)

- 637 Optical pressure sensors for high-pressure–high-temperature studies in a diamond
638 anvil cell. *High Pressure Research*, 27, 447–463.
- 639 DePaolo, D.J. (2015) Sustainable Carbon Emissions: The Geologic Perspective. *MRS*
640 *Energy & Sustainability*, 2.
- 641 Facq, S., Daniel, I., Montagnac, G., Cardon, H., and Sverjensky, D.A. (2014) In situ
642 Raman study and thermodynamic model of aqueous carbonate speciation in
643 equilibrium with aragonite under subduction zone conditions. *Geochimica et*
644 *Cosmochimica Acta*, 132, 375–390.
- 645 Facq, S., Daniel, I., Montagnac, G., Cardon, H., and Sverjensky, D.A. (2016) Carbon
646 speciation in saline solutions in equilibrium with aragonite at high pressure.
647 *Chemical Geology*, 431, 44–53.
- 648 Farfan, G., Wang, S., Ma, H., Caracas, R., and Mao, W.L. (2012) Bonding and structural
649 changes in siderite at high pressure. *American Mineralogist*, 97, 1421–1426.
- 650 Farfan, G.A., Boulard, E., Wang, S., and Mao, W.L. (2013) Bonding and electronic
651 changes in rhodochrosite at high pressure. *American Mineralogist*, 98, 1817–1823.
- 652 Farsang, S., Facq, S., and Redfern, S.A.T. (2018) Raman modes of carbonate minerals as
653 pressure and temperature gauges up to 6 GPa and 500 °C. *American Mineralogist*,
654 103, 1988–1998.
- 655 Farsang, S., Widmer, R.N., and Redfern, S. (2021). High-pressure and high-temperature

- 656 vibrational properties and anharmonicity of carbonate minerals up to 6 GPa and
657 500 °C by Raman spectroscopy. *American Mineralogist*, 106, 581-598.
- 658 Fiquet, G., Guyot, F., Kunz, M., Matas, J., Andrault, D., and Hanfland, M. (2002)
659 Structural refinements of magnesite at very high pressure. *American Mineralogist*,
660 87, 1261–1265.
- 661 Gillet, P., Biellmann, C., Reynard, B., and McMillan, P. (1993) Raman spectroscopic
662 studies of carbonates Part I: High-pressure and high-temperature behaviour of
663 calcite, magnesite, dolomite and aragonite. *Physics and Chemistry of Minerals*, 20,
664 1–18.
- 665 Gillet, P., Cléac’h, A.L., and Madon, M. (1990) High-Temperature Raman-Spectroscopy
666 of SiO₂ and GeO₂ Polymorphs-Anharmonicity and Thermodynamic Properties at
667 High-Temperatures. *Journal of Geophysical Research*, 95, 21635–21655.
- 668 Gillet, P., Guyot, F., and Malezieux, J.M. (1989) High-pressure, high-temperature Raman
669 spectroscopy of Ca₂GeO₄ (olivine form): Some insights on anharmonicity. *Physics*
670 *of the Earth and Planetary Interiors*, 58, 141–154.
- 671 Gillet, P., Hemley, R.J., and McMillan, P.F. (1998) Vibrational properties at high
672 pressures and temperatures. *Ultrahigh-pressure mineralogy*, 525–590.
- 673 Goncharov, A.F., Zaug, J.M., Crowhurst, J.C., and Gregoryanz, E. (2005) Optical
674 calibration of pressure sensors for high pressures and temperatures. *Journal of*

- 675 Applied Physics, 97.
- 676 Hazen, R. M., Downs, R. T., Jones, A. P., and Kah, L. (2013) Carbon Mineralogy and
677 Crystal Chemistry. *Reviews in Mineralogy & Geochemistry*, 75, 7–46.
- 678 Hazen, R. M., R. T. Downs, A. P. Jones, and L. Kah (2013) Carbon mineralogy and
679 crystal chemistry, *Rev. Mineral. Geochem.*, 75, 7–46
- 680 Isshiki, M., Irifune, T., Hirose, K., Ono, S., Ohishi, Y., Watanuld, T., Nishibori, E., Takata,
681 M., and Sakata, M. (2004) Stability of magnesite and its high-pressure form in the
682 lowermost mantle. *Nature*, 427, 60–63.
- 683 Javoy, M. (1997) The major volatile elements of the Earth: Their origin, behaviour, and
684 fate. *Geophysical Research Letters*, 24, 177–180.
- 685 Kaminsky, F.V. and Wirth, R. (2011) Iron carbide inclusions in lower-mantle diamond
686 from Juina, Brazil. *The Canadian Mineralogist*, 49, 555–572.
- 687 Kang, N., Schmidt, M.W., Poli, S., Franzolin, E. and Connolly, J.A.D. (2015) Melting of
688 siderite to 20 GPa and thermodynamic properties of FeCO₃-melt. *Chemical Geology*,
689 400, 34–43.
- 690 Kissinger, H.E., McMurdie, H.F., and Simpson, B.S. (1956) Thermal decomposition of
691 manganous and ferrous carbonates. *Journal of the American Ceramic Society*, 39,
692 168–172.
- 693 Klein, C. (1978) Regional metamorphism of proterozoic iron-formation, Labrador Trough,

- 694 Canada. American Mineralogist, 63, 898–912.
- 695 ——— (2005) Some Precambrian banded iron-formations (BIFs) from around the world:
696 Their age, geologic setting, mineralogy, metamorphism, geochemistry, and origin.
697 American Mineralogist, 90, 1473–1499.
- 698 Klotz, S., Chervin, J.-C., Munsch, P., and Marchand, G. L. (2009) Hydrostatic limits of
699 11 pressure transmitting media. Journal of Physics D: Applied Physics, 42, 75,413.
- 700 Laverne, C. (1993) Occurrence of siderite and ankerite in young basalts from the
701 Galapagos spreading center (DSDP hole-506G and hole-507B). Chemical Geology,
702 106, 27–46.
- 703 Lavina, B., Dera, P., Downs, R.T., Prakapenka, V., Rivers, M., Sutton, S., and Nicol, M.
704 (2009) Siderite at lower mantle conditions and the effects of the pressure-induced
705 spin-pairing transition. Geophysical Research Letters, 36, L23306.
- 706 Lavina, B., Dera, P., Downs, R.T., Yang, W., Sinogeikin, S., Meng, Y., Shen, G., and
707 Schiferl, D. (2010) Structure of siderite FeCO₃ to 56 GPa and hysteresis of its
708 spin-pairing transition. Physical Review B, 82, 064110
- 709 Li, L. and Fei, Y. (2003) Experimental constraints on core composition. In R.W. Carlson,
710 Ed., The Mantle and Core, 2nd edition, Volume 2, p. 521–546. Treatise on
711 Geochemistry, Elsevier, Amsterdam.
- 712 Liang, W., Yin, Y., Li, Zeming, Li, R., Li, L., He, Y., Dong, H., Li, Zengsheng, Yan, S.,

- 713 Zhai, S., and others (2018) Single crystal growth, crystalline structure investigation
714 and high-pressure behavior of impurity-free siderite (FeCO₃). Physics and
715 Chemistry of Minerals, 45, 831–842.
- 716 Lin, J.-F., Liu, J., Jacobs, C., and Prakapenka, V.B. (2012) Vibrational and elastic
717 properties of ferromagnesite across the electronic spin-pairing transition of iron.
718 American Mineralogist, 97, 583–591
- 719 Litasov, K.D., Fei, Y., Ohtani, E., Kuribayashi, T., and Funakoshi, K. (2008) Thermal
720 equation of state of magnesite to 32 GPa and 2073 K. Physics of the Earth and
721 Planetary Interiors, 168, 191–203.
- 722 Litasov, K., Shatskiy, A., Podborodnikov, I., Arefiev, A. (2020) Phase diagrams of
723 carbonate materials at high pressures, with implications for melting and carbon
724 cycling in the deep Earth. In C. Manning, J.F. Lin, W. Mao, Ed., Carbon in Earth's
725 Interior, chapter 14, p. 137–165. John Wiley & Sons Inc, American Geophysical
726 Union.
- 727 Liu, J., Caracas, R., Fan, D., Bobocoiu, E., Zhang, D., and Mao, W.L. (2016)
728 High-pressure compressibility and vibrational properties of (Ca,Mn)CO₃. American
729 Mineralogist, 101, 2723–2730.
- 730 Liu, J., Lin, J.-F., Mao, Z., and Prakapenka, V.B. (2014) Thermal equation of state and
731 spin transition of magnesiosiderite at high pressure and temperature. American

- 732 Mineralogist, 99, 84–93
- 733 Lobanov, S.S., Goncharov, A.F., and Litasov, K.D. (2015) Optical properties of siderite
734 (FeCO₃) across the spin transition: Crossover to iron-rich carbonates in the lower
735 mantle. American Mineralogist, 100, 1059–1064.
- 736 Manning, C.E. (1994) The solubility of quartz in H₂O in the lower crust and upper mantle.
737 Geochimica et Cosmochimica Acta, 58, 4831–4839.
- 738 Mao, H.K., Xu, J., and Bell, P.M. (1986) Calibration of the ruby pressure gauge to 800
739 kbar under quasi-hydrostatic conditions. Journal of Geophysical Research, 91,
740 4673–4676.
- 741 Matilla, A., Pylkkänen, T., Rueff, J-P., Huotari, S., Vanko, G., Hanfland, M., Lehtinen, M.,
742 and Hämäläinen, K. (2007) Pressure induced magnetic transition in siderite FeCO₃
743 studied by X-ray emission spectroscopy. Journal of Physics: Condensed Matter, 19,
744 386206.
- 745 McDonough, W.F. and Sun, S.-s. (1995) The composition of the Earth. Chemical Geology,
746 120, 223–253.
- 747 Melnik, Y.P. (1964) Theoretical data on the stability of siderite in the process of
748 metamorphism. Translated from Akademiya Nauk Ukrainskoy RSR, 24, 16–29.
- 749 Merlini, M., Hanfland, M., and Gemmi, M. (2015) The MnCO₃-II high-pressure
750 polymorph of rhodocrosite. American Mineralogist, 100, 2625–2629.

- 751 Müller, J., Speziale, S., Efthimiopoulos, I., Jahn, S., and Koch-Müller, M. (2016) Raman
752 spectroscopy of siderite at high pressure: Evidence for a sharp spin
753 transition. *American Mineralogist*, 101, 2638–2644.
- 754 Murnaghan, F.D. (1937) Finite Deformations of an Elastic Solid. *American Journal of*
755 *Mathematics*, 59, 235.
- 756 Nagai, T., Ishido, T. Seto, Y., Nishio-Hamane, D., Sata, N., and Fujino, K. (2010)
757 Pressure-induced spin transition in FeCO₃-siderite studied by X-ray diffraction
758 measurements. *Journal of Physics: Conference Series*, 215, 012002.
- 759 Nagai, T., Ishido, T. Seto, Y., Nishio-Hamane, D., Sata, N., and Fujino, K. (2010)
760 Pressure-induced spin transition in FeCO₃-siderite studied by X-ray diffraction
761 measurements. *Journal of Physics: Conference Series*, 215, 012002.
- 762 Nagai, T., Ishido, T., Seto, Y., Nishio-Hamane, D., Sata, N., and Fujino, K. (2010)
763 Pressure-induced spin transition in FeCO₃-siderite studied by X-ray diffraction
764 measurements. *Journal of Physics: Conference Series*, 215, 012002.
- 765 Ono, S. (2007) High-pressure phase transformation in MnCO₃: a synchrotron XRD study.
766 *Mineralogical Magazine*, 71, 105–111.
- 767 Plank, T. and Manning, C.E. (2019) Subducting carbon. *Nature*, 574, 343–352.
- 768 Rao, K.V.K., and Murthy, K.S. (1970) Thermal expansion of manganese carbonate.
769 *Journal of Materials Science*, 5, 82–83.

- 770 Redfern, S.A.T. (2000) Structural variations in carbonates. *Reviews in Mineralogy and*
771 *Geochemistry*, 41, 289–308.
- 772 Robie, R.A., Haselton, H.T., and Hemingway, B.S. (1984) Heat capacities and entropies
773 of rhodochrosite (MnCO_3) and siderite (FeCO_3) between 5 and 600 K. *American*
774 *Mineralogist*, 69, 349–357.
- 775 Rutt, H.N., and Nicola, J.H. (1974) Raman spectra of carbonates of calcite structure.
776 *Journal of Physics C: Solid State Physics*, 7, 4522–4528.
- 777 Santillán, J., and Williams, Q. (2004) A high-pressure infrared and X-ray study of FeCO_3
778 and MnCO_3 : comparison with $\text{CaMg}(\text{CO}_3)_2$ -dolomite. *Physics of the Earth and*
779 *Planetary Interiors*, 143, 291–304.
- 780 Schiferl, D., Nicol, M., Zaug, J.M., Sharma, S.K., Cooney, T.F., Wang, S.-Y., Anthony,
781 T.R., and Fleischer, J.F. (1997) The diamond $^{13}\text{C}/^{12}\text{C}$ isotope Raman pressure sensor
782 system for high-temperature/pressure diamond-anvil cells with reactive samples.
783 *Journal of Applied Physics*, 82, 3256–3265.
- 784 Scott, H.P., Hemley, R.J., Mao, H.-K., Herschbach, D.R., Fried, L.E., Howard, W.M., and
785 Bastea, S. (2004) Generation of methane in the Earth's mantle: In situ high
786 pressure–temperature measurements of carbonate reduction. *Proceedings of the*
787 *National Academy of Sciences of the United States of America*, 101, 14023–14026.
- 788 Seto, Y., Hamane, D., Nagai, T., and Fujino, F. (2008) Fate of carbonates within oceanic

- 789 plates subducted to the lower mantle, and a possible mechanism of diamond
790 formation. *Physics and Chemistry of Minerals*, 35, 223–229.
- 791 Sherman, D.M. (2009) Electronic structures of siderite (FeCO_3) and rhodochrosite
792 (MnCO_3): Oxygen K-edge spectroscopy and hybrid density functional
793 theory. *American Mineralogist*, 94, 166–171.
- 794 Shi, W., Fleet, M.E., and Shieh, S.R. (2012) High-pressure phase transitions in Ca-Mn
795 carbonates $(\text{Ca,Mn})\text{CO}_3$ studied by Raman spectroscopy. *American Mineralogist*, 97,
796 999–1001.
- 797 Spivak, A., Solopova, N., Cerantola, V., Bykova, E., Zakharchenko, E., Dubrovinsky, L.,
798 and Litvin, Y. (2014) Raman study of MgCO_3 - FeCO_3 carbonate solid solution at
799 high pressure up to 55 GPa. *Physics and Chemistry of Minerals*, 41, 633–638.
- 800 Stewart, E.M., Ague, J.J., Ferry, J.M., Schiffries, C.M., Tao, R.B., Isson, T.T., and
801 Planavsky, N.J. (2019) Carbonation and decarbonation reactions: Implications for
802 planetary habitability. *American Mineralogist*, 104, 1369-1380.
- 803 Tao, R., Fei, Y. and Zhang, L. (2013) Experimental determination of siderite stability at
804 high pressure. *American Mineralogist*, 98, 1565-1572.
- 805 Tropper, P., and Manning, C.E. (2007) The solubility of corundum in H_2O at high
806 pressure and temperature and its implications for Al mobility in the deep crust and
807 upper mantle. *Chemical Geology*, 240, 54–60.

- 808 Wang, M., Shi, G., Qin, J., and Bai, Q. (2018) Thermal behavior of calcite-structure
809 carbonates from a powder X-ray diffraction study between 83 and 618 K. European
810 Journal of Mineralogy, 30, 939–949.
- 811 Wood, B.J., Pawley, A., and Frost, D.R. (1996) Water and carbon in the earth's
812 mantle. Philosophical transactions of the Royal Society of London, 354, 1495–1511.
- 813 Yui, S. (1966) Decomposition of siderite to magnetite at lower oxygen fugacities: a
814 thermochemical interpretation and geological implications. Economic Geology, 61,
815 768–776
- 816 Zhang, J., and Reeder, R.J. (1999) Comparative compressibilities of calcite-structure
817 carbonates: Deviations from empirical relations. American Mineralogist, 84, 861–
818 870.
- 819 Zhang, J., Martinez, I., Guyot, F., and Reeder, R.J. (1998) Effects of Mg-Fe²⁺ substitution
820 in calcite-structure carbonates: Thermoelastic properties. American Mineralogist, 83,
821 280–287.
- 822 Zhao, C., Li, H., Jiang, J., He, Y., and Liang, W. (2018) Phase transition and vibration
823 properties of MnCO₃ at high pressure and high-temperature by Raman spectroscopy.
824 High Pressure Research, 38, 212–223.
- 825 Zhao, C., Li, H., Wang, Y., Jiang, J., and He, Y. (2017) SrB₄O₇:Sm²⁺: an optical sensor
826 reflecting non-hydrostatic pressure at high-temperature and/or high pressure in a

827 diamond anvil cell. High Pressure Research, 37, 18–27.

828

829

FIGURES CAPTIONS

830 **Figure 1:** The high- T diamond-anvil cell with Ni-Cr heater coil around the diamond
831 anvils and thermocouple touching one of the diamond anvils.

832

833 **Figure 2:** Representative Raman spectra of siderite (a) and rhodochrosite (b) collected
834 over a range of P - T conditions.

835

836 **Figure 3:** Frequency evolution of the traced vibrational modes of siderite (a) and
837 rhodochrosite (b) as a function of T at atmospheric P . Polynomial fits are shown as
838 described in the text. The experimental uncertainties are given but generally lie within the
839 size of the data marker.

840

841 **Figure 4:** Frequency evolution of the traced vibrational modes of siderite (a) and
842 rhodochrosite (b) as a function of P at room T . Linear fits are shown as described in the
843 text. The experimental uncertainties are given, but generally lie within the size of the data
844 marker.

845

846 **Figure 5:** (a-b) Frequency shift of the traced L mode of siderite (a) and rhodochrosite (b)
847 as a coupled function of P and T and their polynomial fitting surface. (c-d) P - T diagrams
848 showing contours of the L mode Raman band of siderite (c) and rhodochrosite (d).

849

850 **Figure 6:** Difference in predicted pressures by considering P - T cross effects and without
851 considering the impacts of siderite (a) and rhodochrosite (b). $\Delta P = P$ (without cross
852 effects) – P (with cross effects).

853

854 **Figure 7:** Raman shifts of siderite (a) and rhodochrosite (b) as a function of pressure at
855 ambient temperature up to 47 GPa to show a nonlinear migration at higher pressure and
856 peak splitting. The shaded area indicates the approximate phase transition pressures. The
857 color change of HS state (clear) to LS state (green) of siderite is also attached to (a).

858

859 **Figure OM1:** The relationship between $\delta v_i/\delta P$ and pressure range of fit for siderite (a)
860 and rhodochrosite (b) if assuming a linear relationship between the peak position and
861 pressure.

862

863 **Figure OM2:** Difference between the measured pressure and calculated pressure using
864 Eq. 14 for different modes or Eq. 22 for siderite. (a) shows the relationship between

865 deviation and pressure. (b-d) shows the deviation calculated by Eq. 14 of L (b) and v_1 (c)
866 mode or Eq. 22 of v_1 mode (d) in the P - T space.

867

868 **Figure OM3:** Difference between the measured pressure and calculated pressure using
869 Eq. 14 for different modes or Eq. 22 for rhodochrosite. (a) shows the relationship
870 between deviation and pressure. (b-f) shows the deviation calculated by Eq. 14 of L (b),
871 v_1 (c), v_4 (d) and T (e) mode or Eq. 22 of v_1 mode (f) in the P - T space.

872

873 **Figure OM4:** Raman spectra of siderite (a) and rhodochrosite (b) up to 47 GPa. Blue
874 spectra show HS siderite or MnCO_3 -I, and red spectra show LS siderite or MnCO_3 -II. At
875 46.6 GPa, the empty triangle in (b) marks the occurrence of a small shoulder, which
876 belongs to the first occurring MnCO_3 -II and the black triangle marks the last remaining
877 MnCO_3 -I.

878

879

880

TABLES CAPTIONS

881 **Table 1:** Pressure- and temperature-induced shifts of siderite and rhodochrosite.

882

883 **Table 2:** Mode Grüneisen and anharmonic parameters of siderite.

884

885 **Table 3:** Mode Grüneisen and anharmonic parameters of rhodochrosite.

886

887 **Table 4:** Mode Grüneisen and bulk modulus parameters derived from Raman data by
888 fitting the first-order Murnaghan equation of state.

889

890 **Table 5:** Literature review including methods, composition, and transition pressure for
891 siderite and rhodochrosite.

892

Table 1. Pressure- and temperature-induced shifts of siderite and rhodochrosite

Observed mode	Symmetry	Pressure medium	v_1 (cm ⁻¹)	$\delta v_1/\delta P$ (cm ⁻¹ /GPa)	Pressure range of fit (GPa)	$\delta v_1/\delta T$ (cm ⁻¹ /°C)	Temperature range of fit (°C)	Reference	Calculated formula
Siderite									
External	E_g	Neon	182.86	3.58(2)	0-10	$-2.08(98)\times 10^{-3}-3.12(69)\times 10^{-5}$ (a) / $-6.3(4)\times 10^{-3}$ (b)	20-350	This work	$(Fe_{0.95}Mn_{0.046}Mg_{0.004})CO_3$
		Methanol-ethanol (4:1)	183	3.98(9)	0-6	$1(1)\times 10^{-3}$	25-375	Farsang et al. (2018)	$(Fe_{0.98}Mn_{0.01}Mg_{0.01})CO_3$
		Neon	176	2.51	0-40	-	-	Cerantola et al. (2015)	Synthesis sample, pure
		Neon	181	2.99(2)	0-30	$3.14\times 10^{-4}-2.82\times 10^{-5} / -4.3\times 10^{-3}$	20-300	Liang et al. (2018)	$Fe_{0.9988}CO_3$
External	E_g	Neon	283.49	4.50(3)	0-10	$-1.84(17)\times 10^{-2}+2.08(97)\times 10^{-5} / -1.47(3)\times 10^{-2}$	20-350	This work	$(Fe_{0.95}Mn_{0.046}Mg_{0.004})CO_3$
		Methanol-ethanol (4:1)	284	4.52(5)	0-6	$-1.0(1)\times 10^{-2}$	25-375	Farsang et al. (2018)	$(Fe_{0.98}Mn_{0.01}Mg_{0.01})CO_3$
		Neon	274	3.82	0-40	-	-	Cerantola et al. (2015)	Synthesis sample, pure
		Neon	281	4.01(2)	0-30	$-1.26\times 10^{-2}-1.65\times 10^{-5} / -1.54\times 10^{-2}$	20-300	Liang et al. (2018)	$Fe_{0.9988}CO_3$
		silicone oil	299	3.74	0-35	-	-	Farfan et al. (2012)	$(Fe_{0.76}Mn_{0.15}Mg_{0.09}Ca_{0.01})CO_3$
Internal v_1	A_{1g}	Neon	1085.14	2.51(6)	0-10	$-3.15(63)\times 10^{-3}-2.76(43)\times 10^{-5} / -7.1(3)\times 10^{-3}$	20-350	This work	$(Fe_{0.95}Mn_{0.046}Mg_{0.004})CO_3$
		Methanol-ethanol (4:1)	1085	2.60(7)	0-6	$-3(1)\times 10^{-3}$	25-375	Farsang et al. (2018)	$(Fe_{0.98}Mn_{0.01}Mg_{0.01})CO_3$
		Neon	1077	2.17	0-40	-	-	Cerantola et al. (2015)	Synthesis sample, pure
		Neon	1084	2.46(1)	0-30	$-1.88\times 10^{-3}-3.22\times 10^{-5} / -6.9\times 10^{-3}$	20-300	Liang et al. (2018)	$Fe_{0.9988}CO_3$
		silicone oil	1088	2.20	0-43	-	-	Farfan et al. (2012)	$(Fe_{0.76}Mn_{0.15}Mg_{0.09}Ca_{0.01})CO_3$
Rhodochrosite									
External	E_g	Neon	184.41	3.52(3)	0-10	$-3.99(54)\times 10^{-2}-2.16(96)\times 10^{-5} / -3.63(0)\times 10^{-2}$	20-450	This work	$(Mn_{0.936}Fe_{0.059}Mg_{0.005})CO_3$
		Methanol-ethanol (4:1)	185	3.38(6)	0-6	$-1.98(6)\times 10^{-2}$	25-400	Farsang et al. (2018)	$(Mn_{0.99}Fe_{0.01})CO_3$
		silicone oil	201	2.69	0-15	-	-	Farfan et al. (2013)	$(Mn_{0.976}Fe_{0.012}Mg_{0.004}Ca_{0.002})CO_3$
		Nitrogen	183	2.90(7)	0-16	-	-	Zhao et al. (2018)	$(Mn_{0.976}Fe_{0.011}Mg_{0.001}Ca_{0.003})CO_3$
		Neon	184	2.91(5)	0-45	-	-	Liu et al. (2016)	$(Mn_{0.980}Fe_{0.009}Mg_{0.002}Ca_{0.009})CO_3$
External	E_g	Neon	289.49	4.94(4)	0-10	$-3.11(0)\times 10^{-2}-1.20(0)\times 10^{-5} / -3.37(0)\times 10^{-2}$	20-450	This work	$(Mn_{0.936}Fe_{0.059}Mg_{0.005})CO_3$
		Methanol-ethanol (4:1)	290	4.83(8)	0-6	$-2.93(6)\times 10^{-2}$	25-400	Farsang et al. (2018)	$(Mn_{0.99}Fe_{0.01})CO_3$
		silicone oil	302	4.15	0-15	-	-	Farfan et al. (2013)	$(Mn_{0.976}Fe_{0.012}Mg_{0.004}Ca_{0.002})CO_3$
		Nitrogen	288	4.45(10)	0-16	-	-	Zhao et al. (2018)	$(Mn_{0.976}Fe_{0.011}Mg_{0.001}Ca_{0.003})CO_3$
		Helium	290	3.68(9)	0-45	-	-	Liu et al. (2016)	$(Mn_{0.980}Fe_{0.009}Mg_{0.002}Ca_{0.009})CO_3$
Internal v_4	E_g	Neon	718.81	2.14(1)	0-10	$-1.51(19)\times 10^{-2}-4.14(88)\times 10^{-5} / -8.17(0)\times 10^{-3}$	20-450	This work	$(Mn_{0.936}Fe_{0.059}Mg_{0.005})CO_3$
		Methanol-ethanol (4:1)	718	2.03(4)	0-6	$1.4(8)\times 10^{-3}$	25-400	Farsang et al. (2018)	$(Mn_{0.99}Fe_{0.01})CO_3$
		silicone oil	723	0.95	0-15	-	-	Farfan et al. (2013)	$(Mn_{0.976}Fe_{0.012}Mg_{0.004}Ca_{0.002})CO_3$
		Nitrogen	717	1.49(6)	0-16	-	-	Zhao et al. (2018)	$(Mn_{0.976}Fe_{0.011}Mg_{0.001}Ca_{0.003})CO_3$
		Helium	719	1.28(6)	0-45	-	-	Liu et al. (2016)	$(Mn_{0.980}Fe_{0.009}Mg_{0.002}Ca_{0.009})CO_3$
Internal v_1	A_{1g}	Neon	1085.51	3.36(3)	0-10	$5.39(90)\times 10^{-3}-6.88(45)\times 10^{-5} / -1.03(3)\times 10^{-2}$	20-450	This work	$(Mn_{0.936}Fe_{0.059}Mg_{0.005})CO_3$
		Methanol-ethanol (4:1)	1086	3.34(5)	0-6	$-5.8(7)\times 10^{-3}$	25-400	Farsang et al. (2018)	$(Mn_{0.99}Fe_{0.01})CO_3$
		silicone oil	1100	1.91	0-15	-	-	Farfan et al. (2013)	$(Mn_{0.976}Fe_{0.012}Mg_{0.004}Ca_{0.002})CO_3$
		Nitrogen	1084	2.50(9)	0-16	-	-	Zhao et al. (2018)	$(Mn_{0.976}Fe_{0.011}Mg_{0.001}Ca_{0.003})CO_3$
		Helium	1086	2.17(7)	0-45	-	-	Liu et al. (2016)	$(Mn_{0.980}Fe_{0.009}Mg_{0.002}Ca_{0.009})CO_3$

The result by polynomial fitting (a) and linear fitting (b).

Table 2. Mode Grüneisen and anharmonic parameters of siderite

Raman mode	ν_i (cm ⁻¹)	K_0 (GPa)	K_T (GPa)	α_0 ($\times 10^{-5}$ K ⁻¹)	α (K ⁻¹)	γ_{IT}	γ_{IP}	a_i ($\times 10^{-5}$ K ⁻¹)	$\gamma_{IT(300)}$ ^(b)	$\gamma_{IP(300)}$ ^(c)	$a_{i(300)}$ ($\times 10^{-5}$ K ⁻¹) ^(d)	Reference
T	183	117 ^(a)	117-0.031×(T-300) ^(a)	2.98 ^(a)	$1.76 \times 10^{-5} + 3.46 \times 10^{-8} T$ ^(a)	2.29	1.16	3.38	2.15	0.93	4.56	This work
	183	117		2.98		2.54	-0.15	8.03				Farsang et al. (2018)
	176	117				1.18						Cerantola et al. (2015)
	181	97.5				1.61						Liang et al. (2018)
L	283	117	117-0.031×(T-300)	2.98	$1.76 \times 10^{-5} + 3.46 \times 10^{-8} T$	1.86	1.74	0.35	1.75	1.41	1.28	This work
	284	117		2.98		1.86	1.18	2.03				Farsang et al. (2018)
	274	117				1.16						Cerantola et al. (2015)
	282	97.5				1.39						Liang et al. (2018)
ν_1	1085	117	117-0.031×(T-300)	2.98	$1.76 \times 10^{-5} + 3.46 \times 10^{-8} T$	0.27	0.22	0.15	0.25	0.17	0.29	This work
	1085	117		2.98		0.28	0.09	0.56				Farsang et al. (2018)
	1077	117				0.22						Cerantola et al. (2015)
	1084	97.5				0.22						Liang et al. (2018)

(a) from Zhang et al. (1998); (b) the isothermal equivalent of mode Grüneisen parameter, (c) the isobaric equivalent of mode Grüneisen parameter, and (d) the intrinsic anharmonic parameter calculated at 300 °C with the actual values of ν_i at 300 °C.

Table 3. Mode Grüneisen and anharmonic parameters of rhodochrosite

Raman mode	ν_i (cm ⁻¹)	K_0 (GPa)	K_T (GPa)	α_0 ($\times 10^{-5}$ K ⁻¹)	α (K ⁻¹)	γ_T	γ_P	a_i ($\times 10^{-5}$ K ⁻¹)	$\gamma_{T(250)}$ ^(c)	$\gamma_{P(250)}$ ^(d)	$a_{i(250)}$ ($\times 10^{-5}$ K ⁻¹) ^(e)	Reference
T	184	110 ^(a)	Not found	2.28 ^(b)	$2.29 \times 10^{-5} - 5.56 \times 10^{-8} T + 3.36 \times 10^{-10} T^2$ ^(b)	2.1	8.63	-14.89	2.17	9.26	-15.55	This work
	185	110		2.09		2.01	5.12	-6.51				Farsang et al. (2018)
	184	113				2.37						Liu et al. (2016)
	183	110		2.28		1.74	5.33					Zhao et al. (2018)
L	289	110	Not found	2.28	$2.29 \times 10^{-5} - 5.56 \times 10^{-8} T + 3.36 \times 10^{-10} T^2$	1.88	5.1	-7.34	1.93	5.44	-7.7	This work
	290	110		2.09		1.83	4.84	-6.29				Farsang et al. (2018)
	290	113				1.99						Liu et al. (2016)
	288	110		2.28		1.7	5.01					Zhao et al. (2018)
ν_4	719	110	Not found	2.28	$2.29 \times 10^{-5} - 5.56 \times 10^{-8} T + 3.36 \times 10^{-10} T^2$	0.33	0.5	-0.39	0.33	0.52	-0.42	This work
	718	110		2.09		0.31	-0.09	0.85				Farsang et al. (2018)
	719	113				0.33						Liu et al. (2016)
	717	110		2.28		0.23	0.13					Zhao et al. (2018)
ν_1	1086	110	Not found	2.28	$2.29 \times 10^{-5} - 5.56 \times 10^{-8} T + 3.36 \times 10^{-10} T^2$	0.34	0.42	-0.18	0.34	0.44	-0.21	This work
	1086	110		2.09		0.34	0.25	0.17				Farsang et al. (2018)
	1086	113				0.38						Liu et al. (2016)
	1084	110		2.28		0.25	0.3					Zhao et al. (2018)

(a) from Boulard et al. (2015); (b) from Rao and Murthy (1970); (c) the isothermal equivalent of mode Grüneisen parameter, (d) the isobaric equivalent of mode Grüneisen parameter, and (e) the intrinsic anharmonic parameter calculated at 250 °C with the actual values of ν_i at 250 °C, the temperature dependence of the bulk modulus (K_T) is not found, So K_0 is used in this approximate calculation.

Table 4. Mode gruneisen and bulk modulus parameters derived from Raman data by fitting first-order Murnaghan equation of state.

Mineral		Siderite			Rhodochrosite				
Raman mode		T	L	ν_1	T	L	ν_4	ν_1	
ν_1 (cm ⁻¹)	measured value	183	283	1085	184	289	719	1086	
	by fitting	184	284	1086	185	290	720	1086	
γ_T	by calculation	2.29	1.86	0.27	2.10	1.88	0.33	0.34	
	by fitting	2.41	1.98	0.29	2.30	2.05	0.35	0.39	
R ² of fitting		0.9965	0.9985	0.9915	0.9976	0.9981	0.9847	0.9975	
K_T (GPa)		117-0.031×(T-300) ^(a)			NOT FOUND				
γ_T derived from the fitting		2.05			0.31	1.94	1.95	0.31	0.38
K_T (GPa) derived from the fitting		117-0.02961×(T-20) ^(b)			110-0.01735×(T-20) ^(c)				
R ² of fitting		0.9867			0.9871	0.9949	0.9882	0.9907	
Temperature given (K)		373	573	773					
Evaluation	K_T calculated by (a)	114.7	108.5	102.3					
	K_T calculated by (b)	114.6	108.7	102.8					

(a) from Zhang et al. (1998); (b, c) The unit of T is °C.

Table 5. Literature review including methods, composition, and transition pressure for siderite and rhodochrosite.

Reference	Method	Pressure-transmitting medium	Composition	Transition P (GPa)	Ionic radius (Å)	M-O bond distance (Å)	Outer electron configuration
Siderite							
This work	Raman	Helium	(Fe _{0.95} Mn _{0.046} Mg _{0.004})CO ₃	43.6–46.6			
Müller et al. (2016)	Raman	Neon	(Fe _{0.89} Mn _{0.07} Mg _{0.03} Ca _{0.01})CO ₃	43.3–45.5			
Cerantola et al. (2015)	Raman	Neon	FeCO ₃	40–47			
Lobanov et al. (2015)	UV-VIS	Neon	(Fe _{0.95} Mn _{0.05})CO ₃	43–45			
Spivak et al. (2014)	Raman	Neon	FeCO ₃	40–47			
Liu et al. (2014)	Powder + single-crystal XRD	Neon	(Fe _{0.65} Mg _{0.33} Mn _{0.02})CO ₃	43–47 (single-crystal XRD)	0.78	2.142	3d ⁶
Farfan et al. (2012)	Powder XRD + Raman	None (XRD); silicone oil (Raman)	(Fe _{0.76} Mn _{0.15} Mg _{0.09} Ca _{0.01})CO ₃	46 (XRD); 46–50 (Raman)			
Lin et al. (2012)	Powder + single-crystal XRD + Raman	Neon	(Fe _{0.65} Mg _{0.33} Mn _{0.02})CO ₃	45			
Nagai et al. (2010)	Powder XRD	Argon	N/A	47–50			
Lavina et al. (2010)	Single-crystal XRD	Neon	Near end-member	44–45			
Mattilla et al. (2007)	XES	Argon; None above 40 GPa	(Fe _{0.96} Mn _{0.04})CO ₃	~50			
Rhodochrosite							
This work	Raman	Helium	(Mn _{0.936} Fe _{0.059} Mg _{0.005})CO ₃	from 44 Gpa			
Zhao et al. (2018)	Raman	Nitrogen	(Mn _{0.976} Fe _{0.011} Ca _{0.003} Mg _{0.001})CO ₃	16–32			
Liu et al. (2016)	single-crystal XRD + Raman	Neon (XRD); Helium (Raman)	(Mn _{0.980} Fe _{0.009} Ca _{0.009} Mg _{0.002})CO ₃	45–48 (XRD); 44–47 (Raman)			
Mertini et al. (2015)	Single-crystal XRD	Helium	(Mn _{0.96} Ca _{0.04})CO ₃	44			
Boulard et al. (2015)	Infrared + Powder XRD	KBr (Infrared); NaCl (XRD); NaCl (XRD);	(Mn _{0.976} Fe _{0.012} Ca _{0.002} Mg _{0.004})CO ₃	39 (Infrared); 15–34 (XRD)	0.83	2.195	3d ⁵
Farfan et al. (2013)	XES + Powder XRD + Raman	silicone oil (Raman); None (XES)	(Mn _{0.976} Fe _{0.012} Ca _{0.002} Mg _{0.004})CO ₃	15–30 (XRD); 15–30, 48 (Raman); No (XES)			
Ono (2007)	Powder XRD	None	Mn _{0.999} CO ₃	~ 50			
Santillán and Williams (2004)	Infrared + Powder XRD	KBr (Infrared); None (XRD)	(Mn _{0.77} Fe _{0.09} Ca _{0.07} Mg _{0.07})CO ₃	No			

M-O bond distances are from Rutt and Nicola (1974).

Fig. 1

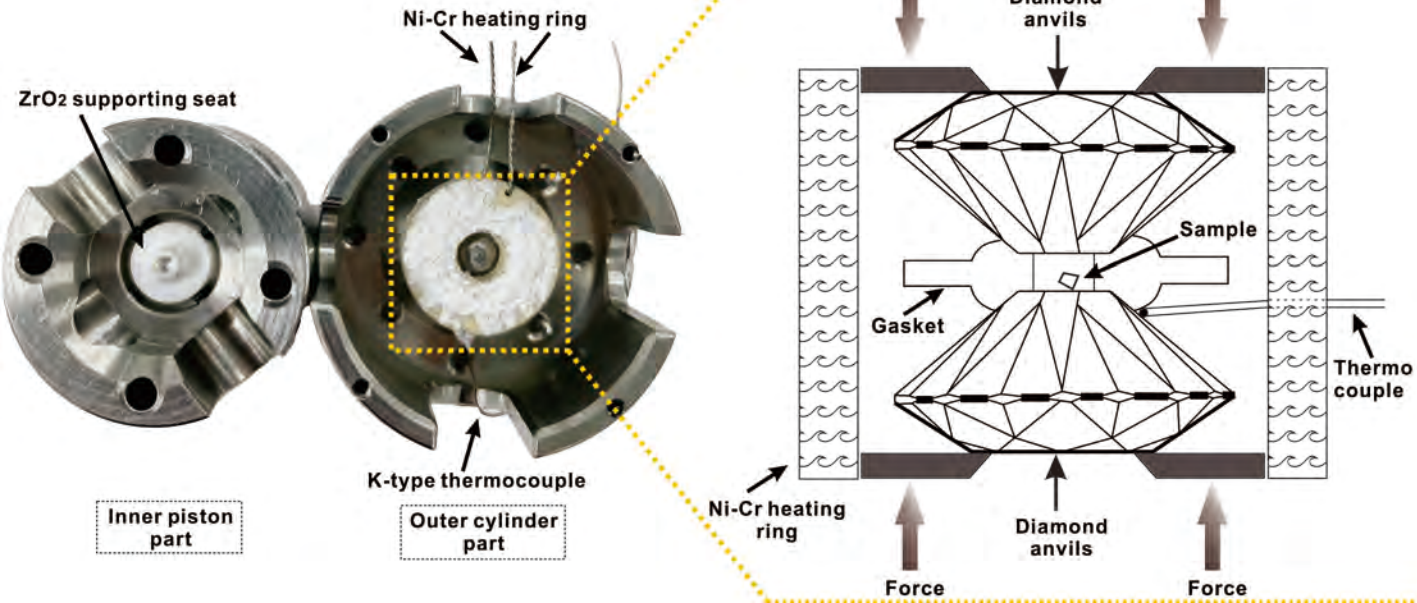


Fig. 2

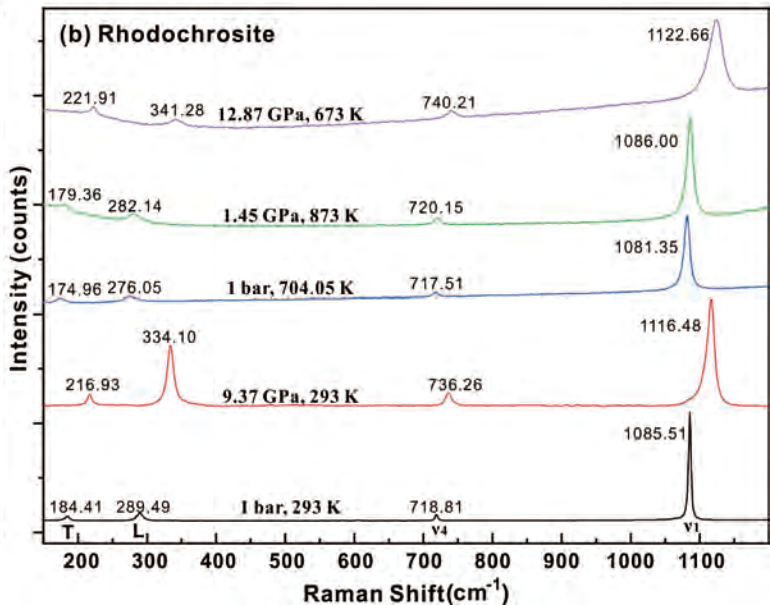
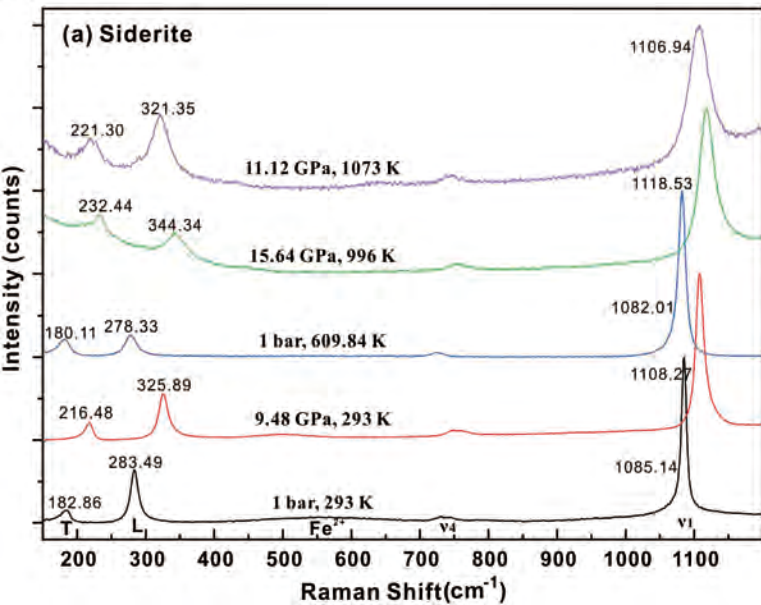


Fig. 3

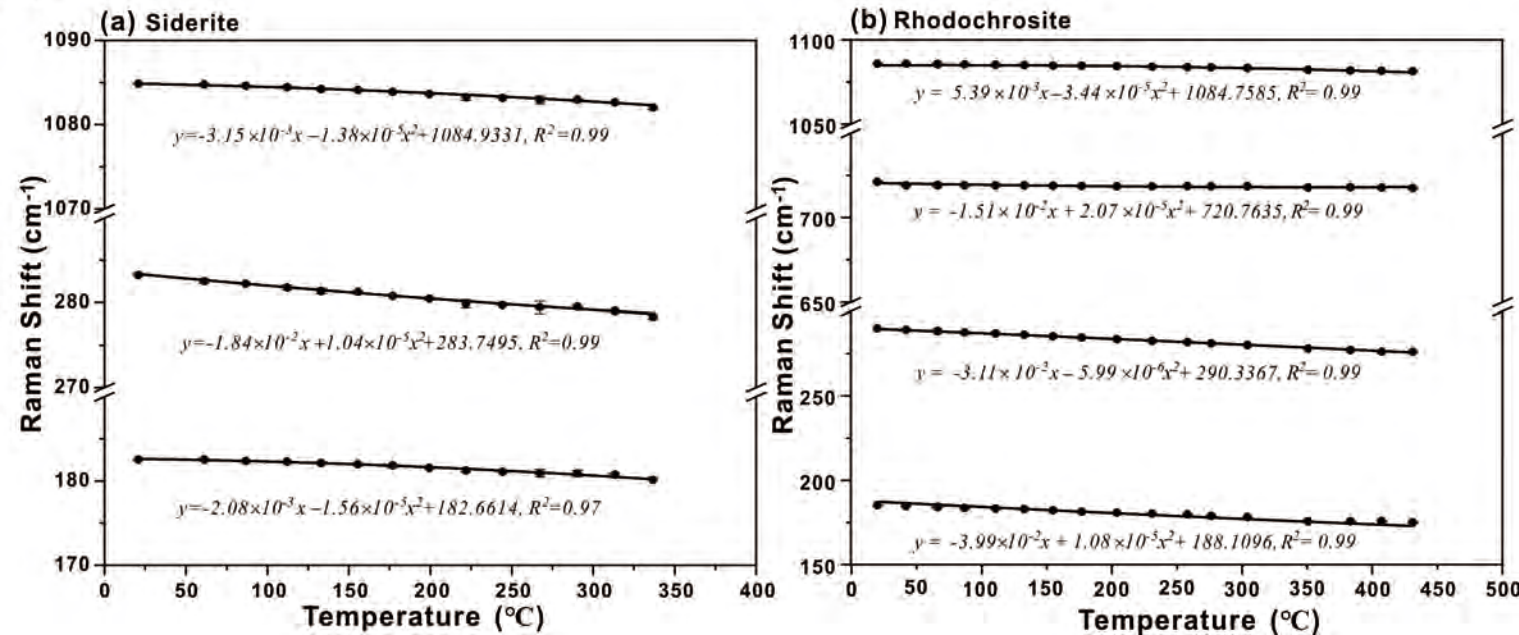


Fig. 4

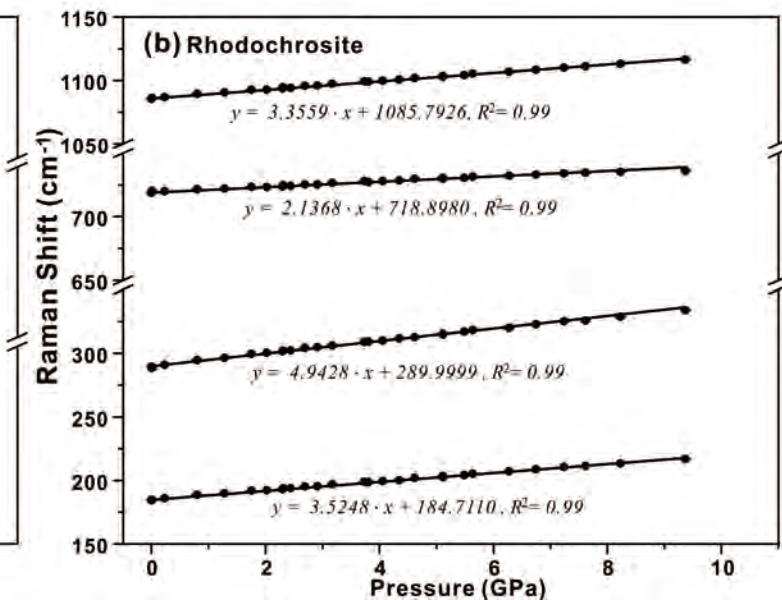
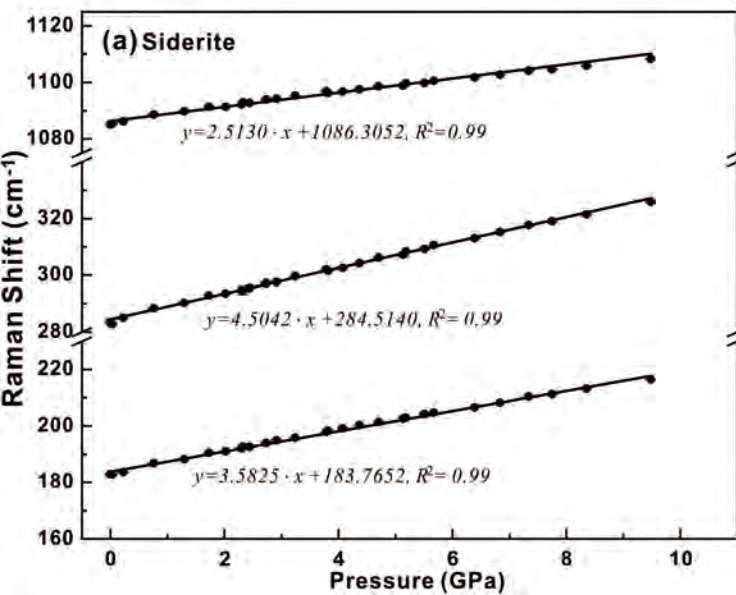


Fig. 5

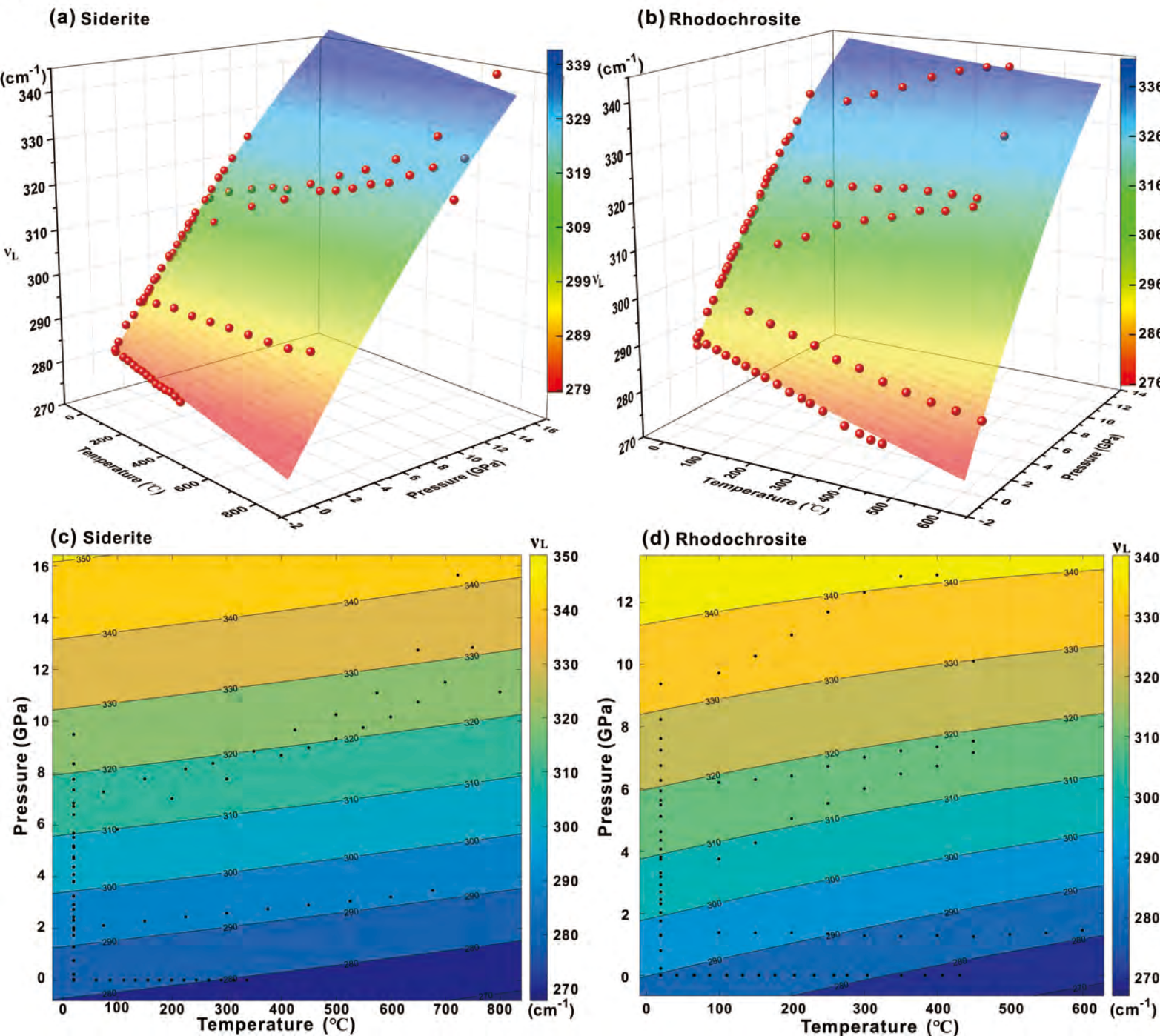


Fig. 6

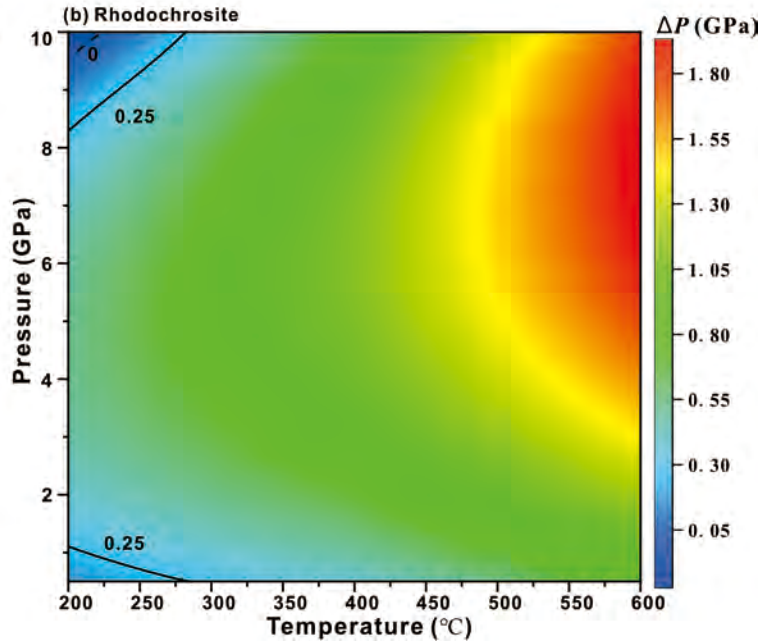
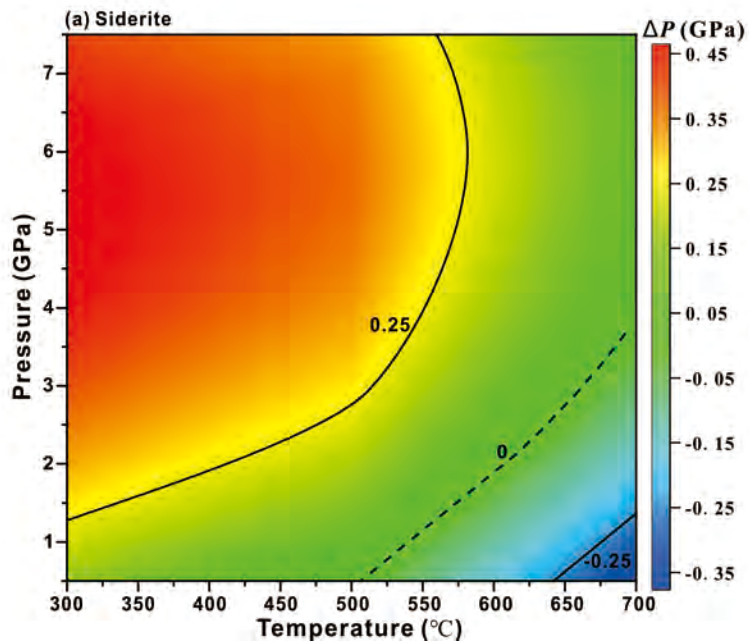


Fig. 7

